JAMES | Journal of Advances in Modeling Earth Systems

RESEARCH ARTICLE
10.1029/2023MS003693

Spatio-Temporal Coarse-Graining Decomposition of the Global Ocean Geostrophic Kinetic Energy

M. Buzzicotti[1], B. A. Storer[2], H. Khatri[3], S. M. Griffies[4,5], and H. Aluie[2,6]

[1]Department of Physics, University of Rome Tor Vergata and INFN, Rome, Italy, [2]Department of Mechanical Engineering, University of Rochester, Rochester, NY, USA, [3]Department of Earth, Ocean and Ecological Sciences, University of Liverpool, Liverpool, UK, [4]NOAA Geophysical Fluid Dynamics Laboratory, Princeton, NJ, USA, [5]Princeton University Atmospheric and Oceanic Sciences Program, Princeton, NJ, USA, [6]Laboratory for Laser Energetics University of Rochester, Rochester, NY, USA

Key Points:

- Coarse-graining, which disentangles flow concurrently in scale and space, reveals hemispheric asymmetry in mesoscale energy-per-area due to boundaries
- Coarse-graining spectra of the time-mean velocity show that most (up to 70%) of its energy resides in "standing" small-scale eddies <500 km
- We estimate that ≈25%–50% of total geostrophic energy is at scales smaller than 100 km, and is un(der)-resolved by pre-SWOT satellite products

Correspondence to:
H. Aluie,
hussein@rochester.edu

Citation:
Buzzicotti, M., Storer, B. A., Khatri, H., Griffies, S. M., & Aluie, H. (2023). Spatio-temporal coarse-graining decomposition of the global ocean geostrophic kinetic energy. *Journal of Advances in Modeling Earth Systems*, *15*, e2023MS003693. https://doi.org/10.1029/2023MS003693

Received 2 MAR 2023
Accepted 11 JUN 2023

Abstract We expand on a recent determination of the first global energy spectrum of the ocean's surface geostrophic circulation (Storer et al., 2022, https://doi.org/10.1038/s41467-022-33031-3) using a coarse-graining (CG) method. We compare spectra from CG to those from spherical harmonics by treating land in a manner consistent with the boundary conditions. While the two methods yield qualitatively consistent domain-averaged results, spherical harmonics spectra are too noisy at gyre-scales (>1,000 km). More importantly, spherical harmonics are inherently global and cannot provide local information connecting scales with currents geographically. CG shows that the extra-tropics mesoscales (100–500 km) have a root-mean-square (rms) velocity of ∼15 cm/s, which increases to ∼30–40 cm/s locally in the Gulf Stream and Kuroshio and to ∼16–28 cm/s in the ACC. There is notable hemispheric asymmetry in mesoscale energy-per-area, which is higher in the north due to continental boundaries. We estimate that ≈25%–50% of total geostrophic energy is at scales smaller than 100 km, and is un(der)-resolved by pre-SWOT satellite products. Spectra of the time-mean circulation show that most of its energy (up to 70%) resides in stationary eddies with characteristic scales smaller than (<500 km). This highlights the preponderance of "standing" small-scale structures in the global ocean due to the temporally coherent forcing by boundaries. By coarse-graining in space and time, we compute the first spatio-temporal global spectrum of geostrophic circulation from AVISO and NEMO. These spectra show that every length-scale evolves over a wide range of time-scales with a consistent peak at ≈200 km and ≈2–3 weeks.

Plain Language Summary Traditionally, "eddies" are identified as time-varying features relative to a background time-mean flow. As such, "mean" does not imply large length-scale. Standing eddies or meanders due to topography have little time-variation, but can have significant energy at small length-scales that are unresolved and need to be parameterized in coarse climate simulations. Similarly, "eddy" or "time-varying" do not imply small length-scale, such as large-scale motions from Rossby waves or fluctuations of the Kuroshio. Another common method is Fourier analysis in "representative" ocean boxes that cannot capture the circulation's planetary scales. We overcome these limitations thanks to recent advances: (a) a method for calculating spectra by coarse-graining, (b) properly defining convolutions on the sphere, which "blur" oceanic flow in a way that preserves its underlying symmetries, opening the door for global "wavelet" analysis and, more generally, spatial coarse-graining, and (c) FlowSieve: an efficient parallel code. We employ coarse-graining in space-time to gain new insights into the global oceanic circulation, including how much energy resides in its different spatial structures and how they vary in time.

1. Introduction

Ocean circulation emerges from a suite of linear and nonlinear dynamical processes that act over a broad range of spatial and temporal scales. The flow field is markedly inhomogeneous and characterized by waves, instabilities, and turbulent eddies, each of which are subject to a variety of energetic sources and sinks. The mesoscale defines a key band of spatial scales where ocean flows are largely geostrophic and where kinetic energy (KE) peaks (Storer et al., 2022; Wunsch, 2007). Correspondingly, it is widely recognized that flow at the ocean mesoscales, and its response to changes in atmospheric forcing, are fundamental to the large-scale circulation and central for regional and global transport of heat and biogeochemical tracers (Ferrari & Wunsch, 2009).

However, significant gaps remain in our understanding of the mesoscale flows and their role in ocean circulation and climate. In particular, from a numerical modeling perspective, despite the ever-increasing ability to conduct simulations with mesoscale eddy-rich Ocean General Circulation Model (OGCM), accurately resolving these scales in routine climate-scale (order centuries and longer) simulations remains the exception rather than the norm (e.g., see Griffies et al., 2015). We are thus confronted with the need for mesoscale eddy parameterizations for the foreseeable future (Pearson et al., 2017).

A central question of physical oceanography, and in particular the eddy parameterization problem, concerns a characterization of flow features according to length-scale. This question motivates the goal of this paper, which is to provide a length-scale decomposition of the global ocean geostrophic KE, and to study the seasonal variations of this decomposition. This goal has previously been out of reach due to limitations of the commonly used Fourier spectral methods, which are unsuited to global ocean analysis due to the complex geometry of ocean basins. We thus make use of a Coarse-Graining (CG) method that does not share the limitations of Fourier analysis. This paper serves to detail the use of coarse-graining for the purpose of decomposing ocean KE, and in so doing we uncover novel features of the ocean surface circulation as a function of length and time scales.

1.1. Fourier Methods for the Ocean

It is common to quantify the spectral distribution in scale of ocean KE via Fourier transforms computed either along transects or within regions (e.g., Callies & Wu, 2019; Chen et al., 2015; Fu & Smith, 1996; Rocha et al., 2016; Khatri et al., 2018), as well as to perform time-decomposition of the flow into its frequency spectra (e.g., Arbic et al., 2012; O'Rourke et al., 2018). This approach has rendered great insights into the length and time scales of oceanic motion and the cascade of energy through these scales (Arbic et al., 2013, 2014; Capet et al., 2008; Schlösser & Eden, 2007; Scott & Arbic, 2007; Scott & Wang, 2005; Xu et al., 2011). However, it has notable limitations for the ocean where the spatial domain is generally not periodic, thus necessitating adjustments to the data (e.g., by tapering) before applying Fourier transforms.

Methods to produce an artificially periodic data set can introduce spurious gradients, length-scales, and flow features not present in the original data (Sadek & Aluie, 2018). A related limitation concerns the chosen region size, with this size introducing an artificial upper length scale cutoff. In this manner, no scales are included that are larger than the region size even if larger structures exist in the ocean. Furthermore, the data is typically assumed to lie on a flat tangent plane to enable the use of Cartesian coordinates. However, if the region becomes large enough to sample the earth's curvature, then that puts into question the use of the familiar Cartesian Fourier analysis of sines and cosines.

We have previously compared coarse-graining methods with traditional Fourier methods, and shown that where Fourier methods are valid, both methods agree (Storer et al., 2022). An important advantage of coarse-graining is that it is not limited to an ocean box and allows us to probe length-scales extending to the planet's circumference. Moreover, unlike Fourier analysis in box regions, which cannot account for the global energy in the ocean, coarse-graining satisfies energy conservation (Sadek & Aluie, 2018) as we discuss more below.

Spherical harmonics transforms are an extension of Fourier (spectral) methods to the full globe, and are often used in atmospheric modeling (Satoh, 2004). Spherical harmonics are basis functions that are defined over the entire sphere and are not restricted to the ocean domain. For this reason, oceanographic analysis tends to employ spherical harmonics less often than atmospheric science analysis, due to the presence of continental boundaries. Ocean tide models are a notable exception, with tide models using spherical harmonics in their computation of the self-attraction and loading effects (e.g., Hendershott, 1972; Ray, 1998). Ocean tide models often set ocean quantities such as sea surface height (SSH) to zero over continents, which introduces some Gibbs ringing but this tends to be small because the higher-order spherical harmonics leading to the Gibbs effects are subdominant, weighted by small number (Arbic, 2022; Arbic et al., 2004). During early days of satellite altimetry, there were attempts at utilizing spherical harmonics to characterize the frequency-wavenumber spectrum of the ocean's global circulation (Wunsch, 1991; Wunsch & Stammer, 1995). These studies analyzed SSH anomalies and chose nominal SSH values over land. SSH over land was set to the time average of the zonal mean absolute SSH. However, the authors were aware that their choice for land treatment was somewhat ad hoc, without dynamical justification, as stated in Wunsch and Stammer (1995): "…we make no claim that we have made the best possible choice." It seems that usage of spherical harmonics for analyzing the oceanic circulation was largely abandoned

after these attempts during the early days of satellite altimetry. In this paper, we revisit spherical harmonics transform in Section 3.5 and show that despite its important limitations, the method can yield meaningful results if land is treated in a manner that is consistent with boundary conditions of the ocean's dynamics.

1.2. Eddy and Mean Flow Decomposition: Reynolds Averages

A traditional approach to extract "eddies" from a flow uses time or ensemble averaging. This approach is relatively simple operationally and is in accord with the common practice in atmospheric and oceanic sciences of studying long-term climate means and fluctuations relative to that mean. As part of this decomposition for turbulent flow, we typically utilize the time averaging operator as a Reynolds averaging (RA) operator, whereby the average of a fluctuating quantity vanishes (Vallis, 2017). The choice of Reynolds decomposition by time averaging is largely based on practical considerations, with ensemble averages being unavailable for most applications (although see (Uchida et al., 2021) for a recent example with fine resolution regional ocean simulations).

Within the traditional decomposition, time-mean or ensemble-mean do not necessarily imply a large length-scale flow as we shall discuss in this paper. For example, standing eddies or stationary meanders due to topography (Youngs et al., 2017) have little temporal or statistical fluctuations but can have spatial structure at length-scales $\mathcal{O}$(100)km or smaller. Similarly, within a Reynolds decomposition, "eddy" does not necessarily imply small length-scale. For example, a time averaging based decomposition would ascribe eddying motion to large-scale Rossby waves (Kessler, 1990) or variations in the Kuroshio Current's path (Kawabe, 1995).

By construction, a Reynolds decomposition into a mean and an "eddy" limits our ability to analyze temporal variability, from intra-annual to inter-annual (Bryan et al., 2014; Griffies et al., 2015), of the multiscale coupling and evolution of different length-scales, including those that need to be resolved/predicted in global climate (coarse-grid) models. Therefore, it offers limited guidance for coarse-resolution models and no control over the specific physical length which partitions oceanic flow into "large" and "small." In other words, the set of length-scales constituting the large-scale flow cannot be varied/controlled to be consistent with those length-scales resolved in a coarse climate simulation. In this sense, the traditional mean-eddy decomposition cannot help with on-going efforts to develop "scale-aware" parameterizations (Jansen et al., 2019; Pearson et al., 2017; Ringler et al., 2013; Zanna et al., 2017), including those using data-driven or machine learning approaches (Ross et al., 2023; Ryzhov et al., 2020).

1.3. Empirical Orthogonal Functions

Empirical Orthogonal Functions (EOFs) offer yet another approach for decomposing the oceanic flow by projecting onto orthogonal basis functions or "empirical modes" that are derived from the data itself. EOF is also known as Karhunen-Loeve decomposition, Principal Component Analysis or Proper Orthogonal Decomposition in other fields (Kac & Siegert, 1947; Karhunen, 1947; Loeve, 1948), and was introduced to meteorology by Lorenz (1956).

EOF analysis is commonly used as a data reduction technique since it offers the most efficient statistical compression of the data field (Thomson & Emery, 2001). This is because the basis functions are derived from the statistical analysis of the data and do not necessarily correspond to true dynamical modes, although they have yielded valuable insight into the oceanic dynamics on climate scales (e.g., Di Lorenzo et al., 2008; Trenberth, 1975). The limitation of EOFs stems from our lack in understanding of the dynamics governing the basis functions. Moreover, it is difficult to associate EOFs with lengthscales or timescales since each empirical mode lumps together variations over all frequency and wavenumber bands. This approach muddles the interpretation of EOF spectra and their connection to spectral slopes predicted by theory (Uchida et al., 2021).

1.4. Coarse-Graining

In order to understand the multiscale nature of oceanic flows, while simultaneously resolving them in space and in time, we use a "coarse-graining" framework that is relatively new in physical oceanography (Aluie et al., 2018; Barkan et al., 2021; Busecke & Abernathey, 2019; Contreras et al., 2023; Haigh et al., 2021; Khani & Dawson, 2023; Khatri et al., 2023; Loose et al., 2023; Rai et al., 2021; Schubert et al., 2020; Srinivasan et al., 2019). It is a very general approach to decompose complex flows, with rigorous foundations initially developed to model

(Germano, 1992; Meneveau, 1994) and analyze (Eyink, 1995, 2005) turbulence. Aluie (2017) provides a theoretical discussion of coarse-graining and its connection to other methods in physics. Wavelet analysis, which has been recently used by Uchida et al. (2023) to analyze quasigeostrophic turbulence, can be regarded as a special case of coarse-graining by choosing the convolution kernel to be a wavelet (Sadek & Aluie, 2018). The approach has been recently generalized to account for the spherical geometry of flow on Earth (Aluie, 2019), and applied to study the nonlinear cascade in the North Atlantic from an eddying simulation (Aluie et al., 2018).

The coarse-graining framework is very useful from the standpoint of ocean subgrid scale parameterizations (Fox-Kemper et al., 2011; Grooms et al., 2021; Haigh et al., 2020; Jansen et al., 2019; Khani et al., 2019; Stanley et al., 2020; Zanna et al., 2017). Namely, it provides a theoretical basis for constructing subgrid closures that faithfully reflect the dynamics at unresolved scales. A primary objective in ocean modeling is practical: an accurate subgrid parameterization that is numerically stable. Significant advances have been achieved in this regard in the fluid dynamics and turbulence community (Biferale et al., 2019; Buzzicotti, Aluie, et al., 2018; Buzzicotti & Clark Di Leoni, 2020; Buzzicotti, Linkmann, et al., 2018; Di Leoni et al., 2020; Linkmann et al., 2018; Piomelli et al., 1991), and the field of large-eddy simulation (LES) is well-established (Meneveau & Katz, 2000).

Our use of coarse-graining supports the needs of parameterization, but our primary objective is to characterize the fundamental dynamics of the flow at *all* length scales. Even within the wider fluid dynamics community, much less work has been done in this regard, that is, using coarse-graining as a "probe" of the fundamental scale-physics. For example, LES sub-grid parameterization studies are seldom concerned with using coarse-graining to probe the energy pathways across the entire range of scales, such as the cascade (Aluie et al., 2012; Buzzicotti, Aluie, et al., 2018; Buzzicotti, Linkmann, et al., 2018; Buzzicotti & Tauzin, 2021; Eyink, 1995; Eyink & Aluie, 2009; Kelley & Ouellette, 2011; Rivera et al., 2014), forcing (Aluie, 2013; Rai et al., 2021; Zhao et al., 2022), dissipation (Zhao & Aluie, 2018), or the range of coupling between different scales (Aluie & Eyink, 2009; Eyink, 2005).

As an important case in point, despite LES having become a well established field in fluid dynamics since the seminal works of Leonard (1974) and Germano (1992), the idea of using coarse-graining in physical space to extract the energy content at different scales; that is, the spectrum, was only recently established and demonstrated by Sadek and Aluie (2018). This method is central to our calculation here of the spectrum for the oceanic general circulation. A main advantage of coarse-graining is that it allows us to decompose different length scales in a flow, at any geographic location and any instant of time, without relying on assumptions of homogeneity, isotropy or domain periodicity. This generality makes it ideally suited for studying oceanic flows with complex continental boundaries over the entire globe or in any particular regions of interest and at any time.

1.5. Key Results and Outline of This Paper

In this paper we make use of the coarse-graining method on a satellite sea surface product and an OGCM simulation. To directly compare the two products, we focus on geostrophic components of the horizontal surface velocity as diagnosed from sea level. Here, we highlight key novel results from this analysis. First, we show that spectra from coarse-graining and spherical harmonics of the global circulation are consistent but the latter cannot yield spatially local information. We show that the typical velocity of mesoscales is of the order of 15 cm/s, but reaches 30–40 cm/s in western boundary currents and 16–28 cm/s in the ACC. We find notable hemispheric asymmetry in mesoscale energy-per-area, which is higher in the north. This asymmtery is compensated by the south having more energy-per-area at gyre-scales, such that across all (resolved) scales, the two hemispheres have comparable energy-per-area. From our spectra, we can estimate that ≈25%–50% of total geostrophic energy is at scales smaller than 100 km, and is un(der)-resolved by pre-SWOT satellite products. Spectra of the time-mean velocity show that most (up to 70%) energy resides in "standing" small-scale eddies <500 km. This highlights the global prevalence of stationary eddies arising from boundary forcing, which is coherent in time and is distinct from the baroclinic instability that is regarded as the main driver of mesoscales. By coarse-graining in space and time, we compute the first spatio-temporal global spectrum of geostrophic circulation from AVISO and NEMO. These spectra show that every length-scale evolves over a wide range of time-scales with a consistent peak at ≈200 km and ≈3 weeks.

The paper is organized as follows. In Section 2, we present the data products used in our analysis. In Section 3 we give details on the coarse-graining and the RA methods used in this work and we present the comparison between CG and spherical harmonics energy spectra. In Section 4 we discuss the main results from the CG analysis; the

2D spatio-temporal energy spectrum of ocean surface circulation and spectra of the time-mean and fluctuating (or "eddy") components from RA. At the end of Section 4 we compare the surface dynamics spatio-temporal decomposition from satellite and numerical model data. In Section 5 we present our conclusions. Appendix A discusses some technical choices we used when coarse-graining.

2. Satellite and Numerical Model Data

We examine the horizontal geostrophic velocity of surface ocean currents from a global numerical model simulation and from an analysis of satellite sea surface altimetry, focusing on regions to the north and south of the tropics, [15°N–90°N] and [15°S–90°S]. We avoid the tropics since our interest is with the geostrophic flows in the higher latitudes, and only the surface geostrophic current is available from satellite altimetry. Details of the two products are given in the following paragraphs, and both were publicly accessed through the Copernicus Marine Environment Monitoring Service webpage, https://marine.copernicus.eu/services-portfolio/access-to-products/.

2.1. AVISO Analysis of Satellite Altimetry

Geostrophic currents are obtained from the AVISO + analysis of multi-mission satellite altimetry measurements for SSH (Pujol et al., 2016). We used the Level 4 (L4) post-processed data set of daily-averaged geostrophic velocity, gridded at a resolution of $0.25° \times 0.25°$ and spanning from January 2010 to October 2018. Post processing was performed by the Sea Level Thematic Center (SL TAC) data processing system, which processes data from 11 altimeter missions. The product identifier of the AVISO data set used in this work is "SEALEVEL_GLO_PHY_L4_MY_008_047" (https://doi.org/10.48670/moi-00148).

2.2. Numerical Simulation

We analyze 1-day averaged surface geostrophic currents from the NEMO numerical modeling framework, which is coupled to the Met Office Unified Model atmosphere component, and the Los Alamos sea ice model (CICE). The NEMO data set consists of weakly coupled ocean-atmosphere data assimilation and forecast system, with data then published on a uniform 1/12° grid. We use daily-averaged data that spans the 4 years from 2016 to 2019. More details about the coupled data assimilation system used for the production of the NEMO data set can be found in Hewitt et al. (2011), Lea et al. (2015). The specific product identifier of the NEMO data set used here is "GLOBAL_MULTIYEAR_PHY_001_030" (https://doi.org/10.48670/moi-00021).

3. Coarse-Graining for the Ocean

In this section, we discuss the coarse-graining framework and how it is used to partition energy across length scales. We also discuss the traditional approach of decomposition in spherical harmonics and the temporal-based RA, in which the flow is decomposed into time-mean and fluctuating components.

3.1. Basics of Coarse-Graining on the Sphere

For any scalar field, $F(\mathbf{x})$, we can calculate its coarse-grained (or low-pass filtered) version, $\overline{F}_\ell(\mathbf{x})$, by convolving $F(\mathbf{x})$ with a normalized filter kernel $G_\ell(\mathbf{r})$,

$$\overline{F}_\ell(\mathbf{x}) = G_\ell * F(\mathbf{x}) \tag{1}$$

where *, in the context of this work, is convolution on the sphere (Aluie, 2019), $\mathbf{x}$ is geographic location on the globe, and the kernel $G_\ell(\mathbf{x})$ can be any non-negative function that is spatially localized (i.e., it goes to zero fairly rapidly as $\mathbf{x} \to \pm\infty$). The parameter ℓ is a length-scale related to the kernel's "width." We use the notation $\overline{(\cdots)}_\ell$ to denote a coarse-grained field. The kernel is area normalized for all ℓ, so that

$$\int G_\ell(\mathbf{x})\, \mathrm{d}S = 1, \tag{2}$$

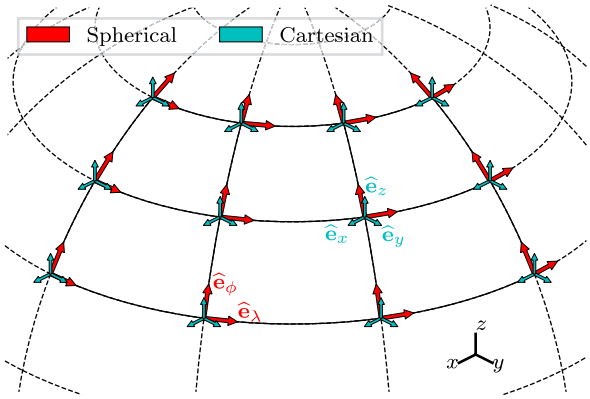

Figure 1. Illustration of [blue arrows] Cartesian velocity basis vectors and [red arrows] Spherical velocity basis vectors at selected latitude/longitude points. While the spherical basis vectors point in different directions at each location, the Cartesian vectors always point in the same direction. When the velocity field is laterally non-divergent (or toroidal) on the spherical surface, using a Cartesian representation of the velocity field allows us to avoid complications from Christoffel symbols (Aluie, 2019). Note that for general (toroidal + poloidal) velocity fields involving overturning, surface divergence, and up/downwelling, the complete coarse-graining formalism of Aluie (2019) is necessary.

where $\mathrm{d}\mathcal{S}$ is the area element on the sphere. Correspondingly, the convolution (1) may be interpreted as an average of the function F within a region of diameter ℓ centered at location $\mathbf{x}$. By construction, at each point in space, $\mathbf{x}$, the coarse-grained field, $\overline{F}_\ell(\mathbf{x})$, contains information about the scale ℓ.

The above formalism holds for coarse-graining scalar fields. To coarse-grain a vector field on a sphere generally requires more work (Aluie, 2019). However, since we are concerned only with the surface geostrophic velocity, $\mathbf{u}(\mathbf{x}, t)$, in this work, it greatly simplifies our analysis. We assume the geostrophic velocity is non-divergent on the two-dimensional spherical surface, so that it is related to the geostrophic stream-function ψ via

$$\mathbf{u} = \hat{\boldsymbol{e}}_r \times \nabla\psi, \tag{3}$$

with $\hat{\boldsymbol{e}}_r$ the radial unit vector in spherical coordinates, $\psi = \eta g/f$, g is the gravitational acceleration, η the free SSH, and the Coriolis parameter, $f = 2\,\Omega\sin(\phi)$, is a function of latitude ϕ, where Ω is Earth's spin rate.

Aluie (2019) showed that for non-divergent vector fields such as in Equation 3, coarse-graining $\mathbf{u}$ is equivalent to coarse-graining each of its Cartesian components. We therefore transform the vector from spherical (u_r, u_λ, u_ϕ) to planetary Cartesian coordinates (u_x, u_y, u_z) via:

$$\begin{aligned} u_x &= u_r\cos(\lambda)\cos(\phi) - u_\lambda\sin(\lambda) - u_\phi\cos(\lambda)\sin(\phi) \\ u_y &= u_r\sin(\lambda)\cos(\phi) + u_\lambda\cos(\lambda) - u_\phi\sin(\lambda)\sin(\phi) \\ u_z &= u_r\sin(\phi) + u_\phi\cos(\phi) \end{aligned} \tag{4}$$

where λ, ϕ are longitude and latitude, respectively, and u_λ, u_ϕ are the zonal and meridional velocity components, respectively. The radial velocity component, $u_r = 0$ for the geostrophic flow. The conversion to Cartesian velocity components is necessary since the basis vectors for spherical velocities depend on space, while the Cartesian velocity basis vectors are spatially independent. Figure 1 illustrates the spatial dependence of the velocity basis vectors.

We apply the spherical convolution operation in Equation 1 to each of u_x, u_y, u_z as scalar fields to obtain the corresponding coarse-grained fields $\overline{u_x}$, $\overline{u_y}$, $\overline{u_z}$, then retrieve the coarse-grained velocity, $\overline{\mathbf{u}}_\ell$ in spherical coordinates via

$$\begin{aligned} \text{coarse radial flow} &= \overline{u_x}\cos(\lambda)\cos(\phi) + \overline{u_y}\sin(\lambda)\cos(\phi) + \overline{u_z}\sin(\phi) = 0 \\ \text{coarse zonal flow} &= -\overline{u_x}\sin(\lambda) + \overline{u_y}\cos(\lambda) \\ \text{coarse meridional flow} &= -\overline{u_x}\cos(\lambda)\sin(\phi) - \overline{u_y}\sin(\lambda)\sin(\phi) + \overline{u_z}\cos(\phi). \end{aligned} \tag{5}$$

That the "coarse-grained radial flow" (i.e., "vertical" flow, parallel to gravity) vanishes is not obvious and was proved in Aluie (2019) and demonstrated numerically in Aluie and Teeraratkul (2023). We emphasize that the coarse-graining algorithm we just described is valid only for non-divergent vectors such as $\mathbf{u}$ in Equation 3. Significant errors can arise for a general flow field (Aluie & Teeraratkul, 2023), where the complete coarse-graining formalism of Aluie (2019) is necessary.

We use the coarse-graining kernel

$$G_\ell(\mathbf{x}) = \frac{A}{2}\left(1 - \tanh\left(10\left(\frac{\gamma(\mathbf{x})}{\ell/2} - 1\right)\right)\right), \tag{6}$$

which is essentially a top-hat kernel (Pope, 2001) with graded edges. We use geodesic distance, $\gamma(\mathbf{x})$, between any location $\mathbf{x} = (\lambda, \phi)$ on Earth's surface relative to location (λ_0, ϕ_0) where coarse-graining is being performed, which we calculate using

$$\gamma(\mathbf{x}) = R_{\text{Earth}}\arccos[\sin(\phi)\sin(\phi_0) + \cos(\phi)\cos(\phi_0)\cos(\lambda - \lambda_0)]. \tag{7}$$

with $R_{\text{Earth}} = 6{,}371$ km for Earth's radius. In Equation 6, A is a normalization factor, evaluated numerically, to ensure G_ℓ area integrates to unity as per Equation 2. In general, we are not restricted to this choice of kernel; however, we use it because of its well-defined characteristic width ℓ. Indeed, a convolution with G_ℓ in Equation 6 is a spatial analogue to an ℓ-day running time-average (e.g., see Section 4.4).

3.1.1. Reflected Hemispheres

A basic complication that can arise when considering very large filter scales is that the filter may become incongruous with studying a smaller sub-domain. In this work, we are primarily concerned with the extra-tropical hemispheres: [−90°N, −15°N] and [15°N, 90°N]. However, at very large length scales information from the equatorial band and opposing hemisphere can become introduced through an expanded filter kernel. To resolve this issue, a "reflected hemispheres" approach is used, wherein one hemisphere is reflected and copied onto the other hemisphere, essentially producing a world with two north, or two south hemispheres. This is the same methodology used in our previous work (Storer et al., 2022).

It is worth noting that the reflected hemispheres and equatorial masking would not be necessary in a context where non-geostrophic velocities are considered and a global power spectrum is desired. They are used here because we wish to disentangle the power spectra of the geostrophic flow in the North and South.

3.2. Partitioning the Geostrophic Kinetic Energy

From the coarse-grained horizontal geostrophic velocity field, $\overline{\mathbf{u}}_\ell(\mathbf{x}, t)$, following Equation 1 as prescribed in Aluie (2019), we partition KE into different sets of length-scales:

$$\mathcal{E} = \frac{1}{2}|\mathbf{u}(\mathbf{x}, t)|^2 (\text{bareKE}) \tag{8}$$

$$\mathcal{E}_\ell = \frac{1}{2}|\overline{\mathbf{u}}_\ell(\mathbf{x}, t)|^2 (\text{coarseKE}) \tag{9}$$

$$\mathcal{E}_{<\ell} = \frac{1}{2}\left(\overline{|\mathbf{u}(\mathbf{x}, t)|^2}_\ell - |\overline{\mathbf{u}}_\ell(\mathbf{x}, t)|^2\right) (\text{fineKE}). \tag{10}$$

The "bare KE" in Equation 8 is the KE per unit mass (m^2/s^2) of the original geostrophic flow that includes all scales; "coarse KE" in Equation 9 represents energy of the coarse-grained geostrophic flow at length-scales larger than ℓ; and "fine KE" in Equation 10 accounts for geostrophic energy at scales smaller than ℓ, which we discuss more in the following two paragraphs. Partitioning geostrophic energy across scales is not trivial since one needs to ensure that such quantities are physically valid in the sense described by Germano (1992) and Vreman et al. (1994). In particular, it is important to ensure that the partitioned KE is (a) positive semi-definite (≥ 0) at every $\mathbf{x}$ and every time, and (b) that summing the partitions yields the total energy.

While it is clear that $\mathcal{E}_\ell \geq 0$ in Equation 9, this property is not obvious for $\mathcal{E}_{<\ell}$ in Equation 10. Moreover, it may not be obvious why $\mathcal{E}_{<\ell}$ should represent energy at scales smaller than ℓ. Vreman et al. (1994) showed that $\mathcal{E}_{<\ell} \geq 0$ if $G_\ell \geq 0$, whereas $\mathcal{E}_{<\ell}$ can be negative if the coarse-graining kernel G_ℓ is not positive semi-definite. A proof using convexity of the square function, $(\ldots)^2$, illustrates why the first term $\overline{|\mathbf{u}(\mathbf{x}, t)|^2}_\ell$ in Equation 10 has an overbar rather than defining fine KE as $\left(|\mathbf{u}(\mathbf{x}, t)|^2 - |\overline{\mathbf{u}}_\ell(\mathbf{x}, t)|^2\right)/2$. The proof from Sadek and Aluie (2018) is as follows. When using $G_\ell \geq 0$, coarse-graining $\overline{(\ldots)}_\ell$ is a local averaging operation. From Jensen's inequality (Lieb & Loss, 2001), we know that $\overline{[\mathcal{F}(\mathbf{u})]}_\ell \geq \mathcal{F}\left(\overline{\mathbf{u}}_\ell\right)$ for any convex operation, $\mathcal{F}$. Since $\mathcal{F}(\mathbf{u}) = |\mathbf{u}|^2$ is convex, we are guaranteed that $\overline{|\mathbf{u}(\mathbf{x}, t)|^2}_\ell \geq |\overline{\mathbf{u}}_\ell(\mathbf{x}, t)|^2$ and, therefore, $\mathcal{E}_{<\ell} \geq 0$ if the kernel $G_\ell(r) \geq 0$, which is the case for our study (see Equation 6).

Regarding condition (ii) on the sum of energy partitions, Aluie (2019) proved that (for a normalized G_ℓ) the coarse-graining operation on the sphere in Equation 1 preserves the spatial average of any field, $\left\{\overline{F}_\ell(\mathbf{x})\right\} = \{F(\mathbf{x})\}$, where $\{\ldots\} = (\text{Area})^{-1} \int \mathrm{d}S(\ldots)$. Therefore, we have $\left\{\overline{|\mathbf{u}|^2}_\ell\right\} = \left\{|\mathbf{u}|^2\right\}$. This property guarantees that the sum of coarse KE and fine KE yields the total KE after integrating in space and in the absence of land,

$$\{\mathcal{E}\} = \{\mathcal{E}_\ell\} + \{\mathcal{E}_{<\ell}\}. \tag{11}$$

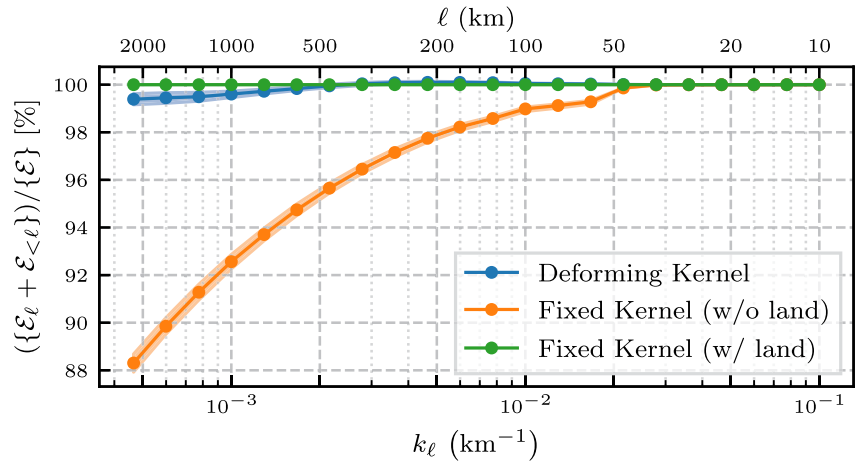

Figure 2. Percentage of total energy recovered by summing the fine and coarse kinetic energy terms in Equation 11 obtained by coarse-graining over the full ocean surface as a function of the filter scale, $k_\ell = 1/\ell$. The three lines correspond to the three approaches described in Section 3.3, namely, filtering with a fixed kernel shape and excluding/including land (orange/green lines) when tallying the total energy. We also coarse-grain with a deformable filter kernel to exclude the filter overlapping land regions (blue line).

Equation 11 justifies our interpretation of $\mathcal{E}_{<\ell}$ as energy at scales smaller than ℓ, since it is the difference between bare and coarse KE, on average, while also being positive locally.

3.3. Treatment of Land-Sea Boundaries

In the above decomposition of energy, a choice has to be made in the presence of land. Storer et al. (2022) provides some discussion on the subject, while here we discuss three possibilities, along with their pros and cons, in more detail.

3.3.1. Deformed Kernel

The "deformed kernel" approach is realized by coarse-graining ocean points near land with a kernel that is deformed or masked to avoid overlapping with land points. Such a deformed kernel must be renormalized to yield an average over just ocean points rather than the whole sphere. The main advantage of this approach is that it treats land as a well-defined boundary that is separate from the ocean regardless of the coarse-graining length-scale. It is also familiar to ocean modelers who routinely mask values over land and do not include such masked values when performing area averages.

However, the deformed kernel has disadvantages that motivate against its use for coarse-graining ocean flows. First, a kernel that is inhomogeneous (i.e., changes shape depending on geographic location) does not conserve domain averages, including the KE of the flow. The reason for this failed conservation is detailed in Appendix A and demonstrated in Figure 2 (blue plot). This figure shows how a kernel that is deformed (via masking) to exclude land does not yield 100% of the total energy, that is, it does not satisfy Equation 11. As a result, it can yield total energy that is either less than 100% (e.g., over scales larger than 500 km in Figure 2) or *greater* than 100% (e.g., between 100 and 400 km in Figure 2).

For some purposes, the total energy values in Figure 2 are fairly close to 100% (deviations less than 1%) so one might argue that the deformed kernel is suitable in practice. Nonetheless, a more basic reason to avoid deformed kernels is that such inhomogeneous kernels (which also include averaging values at adjacent grid-cells or block-averaging on the sphere) do not commute with spatial derivatives. Consequently, the coarse-grained field resulting from a deformed kernel is not guaranteed to satisfy fundamental flow properties exhibited by the unaveraged flow, such as non-divergence, geostrophy, and the vorticity present at various scales. These considerations are further detailed in Aluie et al. (2018) and Aluie (2019).

3.3.2. Fixed Kernel

The "fixed kernel," also used in Figure 2, is homogeneous so that it preserves its shape at all locations. When coarse-graining ocean points near land such that the kernel overlaps land points, we treat land points in a manner consistent with the boundary conditions between land and ocean. For example, if we are coarse-graining the velocity, we treat land as water with zero velocity, which is consistent with the formulation of OGCM where land is often treated as a region of zero velocity. Furthermore, we include these zero land values as part of the coarse-graining operation.

This choice may seem unnatural since we are including unphysical values within the coarse-graining operation. However, it is helpful to think of coarse-graining as an operation analogous to removing one's eyeglasses, rendering an image fuzzy and boundaries less well-defined. When coarse-graining at a scale ℓ, the precise boundary between land and ocean becomes blurred at that scale and its precise location becomes less certain. The coarse-grained velocity, $\overline{\mathbf{u}}_\ell$, can be nonzero within a distance $\ell/2$ beyond the continental boundary over land. Forfeiting exact spatial localization in order to gain scale information is theoretically inevitable due to the uncertainty principle, which prevents the simultaneous localization of data in physical-space and in scale-space (Sogge, 2008; Stein & Weiss, 1971). The main advantage of the "Fixed Kernel" choice is ensuring that coarse-graining and spatial derivatives commute so that it preserves the fundamental physical properties (symmetries) of the flow. Further discussion of these issues can be found in Aluie et al. (2018) and Aluie (2019).

3.3.3. Fixed Kernel With or Without Land

After coarse-graining the velocity field with a fixed kernel, we show in Figure 2 the level of energy conservation if we include or exclude land points from the final tally of KE. We call these, respectively, the "fixed kernel w/ land" and "fixed kernel w/o land." The latter (orange line) highlights how coarse-graining smears energy onto land (within $\ell/2$ distance inland) such that if we exclude land from the final tally, we find some leakage of energy onto land, which increases as the coarse-graining scale ℓ increases. We find energy leakage of the order of 1% at coarse-graining scales <100 km, ≈4% for scales ≲500 km, and up to 12% at scales of order 2,000 km. However, if we choose to include land in our final tally, we are guaranteed to conserve 100% of the energy by satisfying Equation 11, thus ensuring that the energy budget is fully closed. After all, in an ocean model on a discrete grid, the land boundary is only expected to be accurate within a Δx distance from any estimate of the truth, where Δx is analogous to our coarse-graining scale ℓ.

3.3.4. What We Use Here

While we have implemented all three approaches to coarse-graining, unless otherwise stated in this work, we choose the fixed kernel w/land by including land regions that have non-zero velocity (again, as realized through leakage from nearby ocean values). Storer et al. (2022) showed that deformed and fixed kernels yield qualitatively consistent results for spectra. We avoid coarse-graining with a deformed kernel to remain consistent with previous work (Aluie et al., 2018) and with forthcoming studies where we apply coarse-graining to the dynamical equations where commuting with spatial derivatives is essential.

3.4. The Filtering Spectrum

Sadek and Aluie (2018) showed how coarse-graining can be used to extract the energy content at different length scales. They do so by partitioning the velocity into discrete length scale bands rather than the two sets (coarse KE and fine KE) in Equations 9 and 10. The resulting quantity is called the *filtering spectrum*. The filtering spectrum is distinct from the traditional Fourier spectrum, with coarse-graining offering a way to measure energy distributions without relying on a Fourier transform, thus avoiding the limitations noted in Section 1.1.

The filtering spectrum is obtained by differentiating in scale the coarse KE

$$\overline{E}(k_\ell) = \frac{d}{dk_\ell}\{\mathcal{E}_\ell\} = -\ell^2 \frac{d}{d\ell}\{\mathcal{E}_\ell\}, \tag{12}$$

where $k_\ell = 1/\ell$ is the "filtering wavenumber." Sadek and Aluie (2018) showed that the filtering spectrum satisfies energy conservation and that $\overline{E}(k_\ell, t) \geq 0$ when using certain types of kernels (e.g., concave) of which the top-hat kernel is an example. Moreover, Sadek and Aluie (2018) identified the conditions on G_ℓ for $\overline{E}(k_\ell, t)$ to be meaningful in the sense that its scaling agrees with that of the traditional Fourier spectrum (when a Fourier analysis

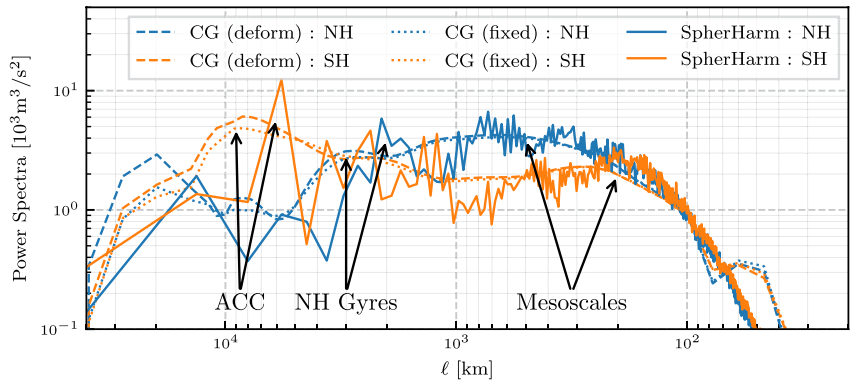

Figure 3. Power Spectra with Spherical Harmonics and Coarse-Graining Power spectra computed using spherical harmonics (solid lines), coarse-graining with a deforming kernel (dashed lines), and coarse-graining with a fixed kernel with land (dotted lines). Reflected hemispheres were used to obtain spectra for NH and SH separately. Note that these spectra were obtained by masking out only a thin strip [2°S, 2°N] and integrating over the domain to allow for the application of spherical harmonic transforms, unlike those of Figure 8 and (Storer et al., 2022) that only integrated over latitudes outside of [15°S, 15°N], explaining the discrepancy in peak locations.

is possible, such as in periodic domains). Below, we shall sometimes refer to $\mathcal{E}_\ell$ as the "cumulative spectrum" following Sadek and Aluie (2018) since it accounts for all energy at scales larger than ℓ. In contrast, $\overline{E}(k_\ell, t)$, is the spectral energy *density* at a specific scale ℓ.

3.5. Comparison With Spherical Harmonics

Our previous results on spectra using CG in Storer et al. (2022) provide justification for using spherical harmonics on the global ocean and a guide for treating land in a manner that is consistent with boundary conditions. For the ocean velocity, the boundary conditions are zero normal velocity (no flow through) and zero tangential velocity (no-slip). Therefore, when using spherical harmonics, we set land to have zero velocity values, similar to what we do with the CG method.

Figure 3 compares spectra from CG to those from spherical harmonics. It uses a single daily average of the AVISO data with spherical harmonics, coarse-grained with a deforming kernel, and coarse-grained with a fixed kernel including land regions. The spherical harmonic analysis was performed using PySHTools (Wieczorek & Meschede, 2018) on the AVISO data with reflected hemispheres.

The two CG methods yield qualitatively consistent domain-averaged results, such as the broad mesoscale peak, the NH gyre peak, and the ACC peak. Small deviations between the deformable and fixed kernels are only visible on the larger scales, where the deformable filter is not expected to conserve total energy. Given these results, we focus on the comparison between the fixed kernel CG and the spherical harmonic spectra. In this case, both spectra integrate to the same total energy. However, the spherical harmonics spectra are too noisy at gyre-scales (>1,000 km). At these large length-scales (low modes), spherical harmonics spectra have poor scale resolution because the eigenmodes are spaced far apart; in integer multiples of the fundamental mode. It is particularly noticeable around the ACC peak at $\ell \approx 10^4$ km. This limitation is shared by Fourier methods in a Cartesian box. This is not a limitation for the CG method of computing spectra since it conserves energy without relying on the orthogonality structure of an eigenbasis in the strict sense (Sadek & Aluie, 2018).

A main disadvantage of spherical harmonics is that they are inherently global and cannot provide local information connecting scales with currents geographically. This becomes apparent in spatial maps, such as those in Figure 4. In coarse-graining, non-zero current velocities only intrude a distance of $\ell/2$ inland from the coast, as evidenced by the thin band of dark colors inside the yellow contour lines (coastlines). Moreover, the band within the yellow contour is dark, which reinforces that very little energy is distributed over land. Even at a 1,000 km filter scale, the majority of land retains identically zero velocity, indicated by white. In contrast, even at a small filter scale, spherical harmonics generate beams of spectral ringing that extend deep into land regions, with non-trivial magnitudes. Worse still, at a 1,000 km filter, the spherical harmonic filtering fills the global

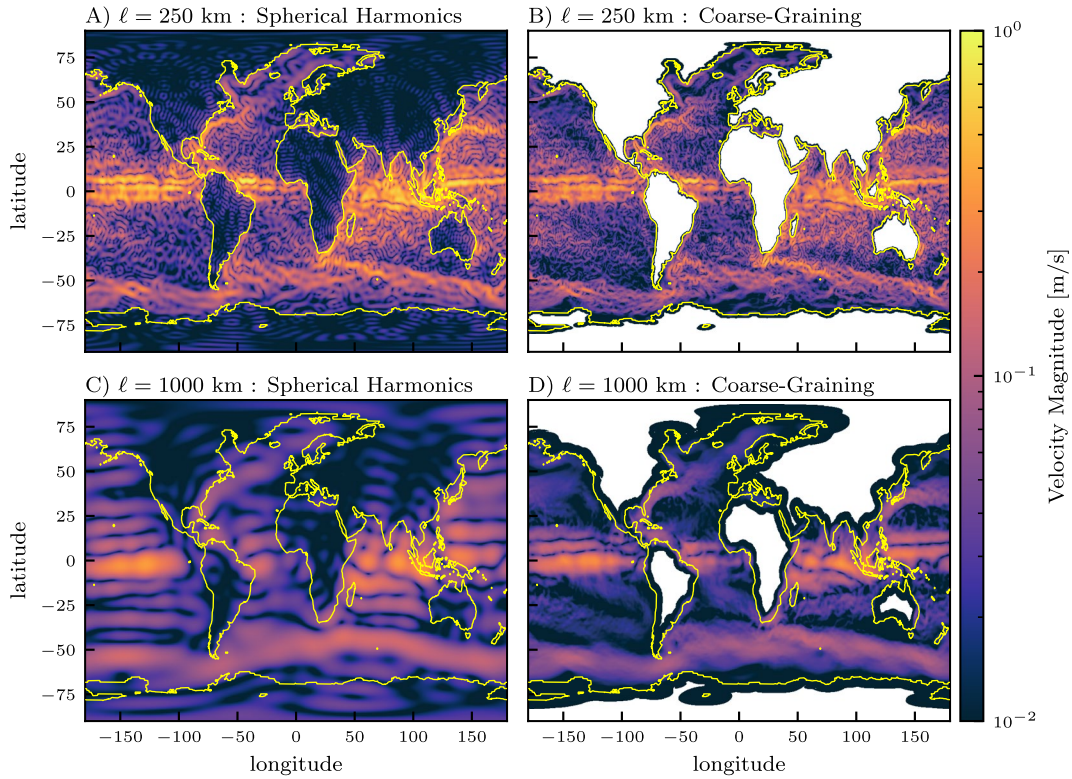

Figure 4. Filtering Maps with Spherical Harmonics and Coarse-Graining Speed of the large-scale AVISO surface currents obtained by [left, AC] spherical harmonics and [right, BD] coarse-graining. Velocity fields are filtered at [top, AB] 250 km and [bottom, CD] 1,000 km. Color maps show velocity magnitude on a logarithmic scale, with white indicating identically zero values. Yellow contours indicate land boundaries in the unfiltered data. Note how filtering with spherical harmonics, even at 250 km, yields non-zero flow over all continents and prominent ringing patterns. This is due to the inherently global nature of spherical harmonics, which makes it challenging to infer spatially local information at different scales.

ocean with zonal bands, even in the more quiescent open oceans. These ringing features are not present under a coarse-graining approach with an appropriately chosen kernel.

In addition, there are practical considerations in regards to comparing coarse-graining with spherical harmonics. Like traditional Fourier methods, spherical harmonics require the input data to conform to fairly strict structures: uniform lat/lon grids, specific resolution aspect ratios, etc. In contrast, coarse-graining is grid agnostic. That is, while the implementation details are different, coarse-graining applies just as well to a uniform lat/lon grid as to a generalized non-uniform triangularization grid. While FlowSieve (Storer & Aluie, 2023), the coarse-graining package used in this work, at present only accepts rectangular (but non-uniform) lat/lon grids, that is a limitation imposed by the current implementation, and not by the underlying methodology.

3.6. Reynolds Averaging

We close this section by reviewing basic properties of RA as realized by time averages.

3.6.1. Basics of Reynolds Averaging

Time averaging separates the flow into a time-average/"mean" and a fluctuating/"eddy" as given by Pope (2001)

$$\langle \mathbf{u} \rangle(\mathbf{x}) = \frac{1}{T} \int_{t_0}^{t_0+T} \mathbf{u}(\mathbf{x}, t) \mathrm{d}t, \tag{13}$$

$$\mathbf{u}'(\mathbf{x}, t) = \mathbf{u}(\mathbf{x}, t) - \langle \mathbf{u} \rangle(\mathbf{x}), \tag{14}$$

where $\langle \mathbf{u} \rangle$ is the mean component, $\mathbf{u}'$ the eddy component, and T represents the entire time record and not just a time window. Two key properties of the Reynolds decomposition are

$$\langle \langle \mathbf{u} \rangle \rangle = \langle \mathbf{u} \rangle \quad \text{and} \quad \langle \mathbf{u}' \rangle = 0, \tag{15}$$

so that the mean of a mean returns the mean (idempotent property) while the mean of the eddy is zero. The resulting mean and eddy KE components are respectively given by

$$MKE(\mathbf{x}) = \frac{1}{2} |\langle \mathbf{u} \rangle|^2(\mathbf{x}), \tag{16}$$

$$EKE(\mathbf{x}, t) = \frac{1}{2} |\mathbf{u}'|^2(\mathbf{x}, t). \tag{17}$$

Notice that the sum of mean and eddy KE is not equal to the total KE. Rather, there is an extra cross term, $\mathbf{u}' \cdot \langle \mathbf{u} \rangle$, needed to close the budget. However, the cross term is not positive definite and it has a zero time average, $\langle \mathbf{u}' \cdot \mathbf{u} \rangle = 0$. Following a RA decomposition, the total energy can be written as

$$\mathcal{E}(\mathbf{x}, t) = EKE(\mathbf{x}, t) + MKE(\mathbf{x}) + \frac{1}{2} \big(\mathbf{u}' \cdot \langle \mathbf{u} \rangle \big)(\mathbf{x}, t). \tag{18}$$

3.6.2. Key Differences Between Reynolds Averaging and Coarse-Graining

A key difference between coarse-graining and Reynolds-averaging is that within RA, applying the averaging operation twice on any field yields the same result whereas that property does not hold for coarse-graining with non-projector kernels, which produce different filtering results when operating multiple times on the same field (Buzzicotti, Aluie, et al., 2018; Buzzicotti, Linkmann, et al., 2018):

$$\langle \langle F \rangle \rangle = \langle F \rangle \quad \text{whereas} \quad \overline{\overline{F}} \neq \overline{F}, \tag{19}$$

where $\langle \cdot \rangle$ denotes time (or Reynolds) averaging and $\bar{\cdot}$ denotes coarse-graining. Another important difference is that a Reynolds average does not provide a control to adjust the partition between the "mean" and "eddy" components. That is, a Reynolds decomposition is not a scale decomposition and this point is illustrated in Section 4.4. Consequently, the time-mean or ensemble-mean flow is not synonymous with large-scale flow, nor does a Reynolds eddy fluctuation directly correspond to a characteristic fine-scale.

To help understand the above points, we emphasize the distinction between time-scale and decorrelation-time for a particular flow feature. While it is generally true that larger (smaller) scales have slower (faster) time-scale dynamics, it is not always true that their decorrelation-time follows this relation. As an example, consider stationary eddies, such as the Mann eddy in the North Atlantic. Such eddies have a small spatial-scale (relative to the gyre or basin) but are persistent in time. As a result, even if the timescale ($\sim \ell/u$) for a structure is small when it is associated with the relatively fast dynamics of eddying flows, it can be highly correlated (or even stationary) in time, so that its contribution to the *MKE* is not completely removed by a time-average. We show this behavior in Sections 4.4 and 4.5.

4. Analysis Results

In this section we present results of the coarse-graining analysis along with a comparison with RA based on time averages. In the second part of this section we present results from coarse-graining in both space and time as a means to characterize the time-scales associated with different length-scales.

4.1. Coarse-Graining the Surface Geostrophic Flow From AVISO

We split the geostrophic KE from AVISO into its fine and coarse-grained components following Equations 9 and 10. For a qualitative appreciation of this decomposition, Figure 5 displays maps of the KE just over the Atlantic using two different filter scales, $\ell = 100$ km in the top row and $\ell = 400$ km in the bottom row. From left to right, panels in Figure 5 show the total KE, $\mathcal{E}$, the coarse energy, $\mathcal{E}_\ell$, and the fine energy, $\mathcal{E}_{<\ell}$. The fine scale KE, $\mathcal{E}_{<\ell}$, represents KE at scales less than ℓ, as represented (or projected) on a grid of resolution $\Delta x \sim \ell$. Notably, as seen in Figure 5, $\mathcal{E}_{<\ell}$ does not have small scale features, which results since there is a filter applied

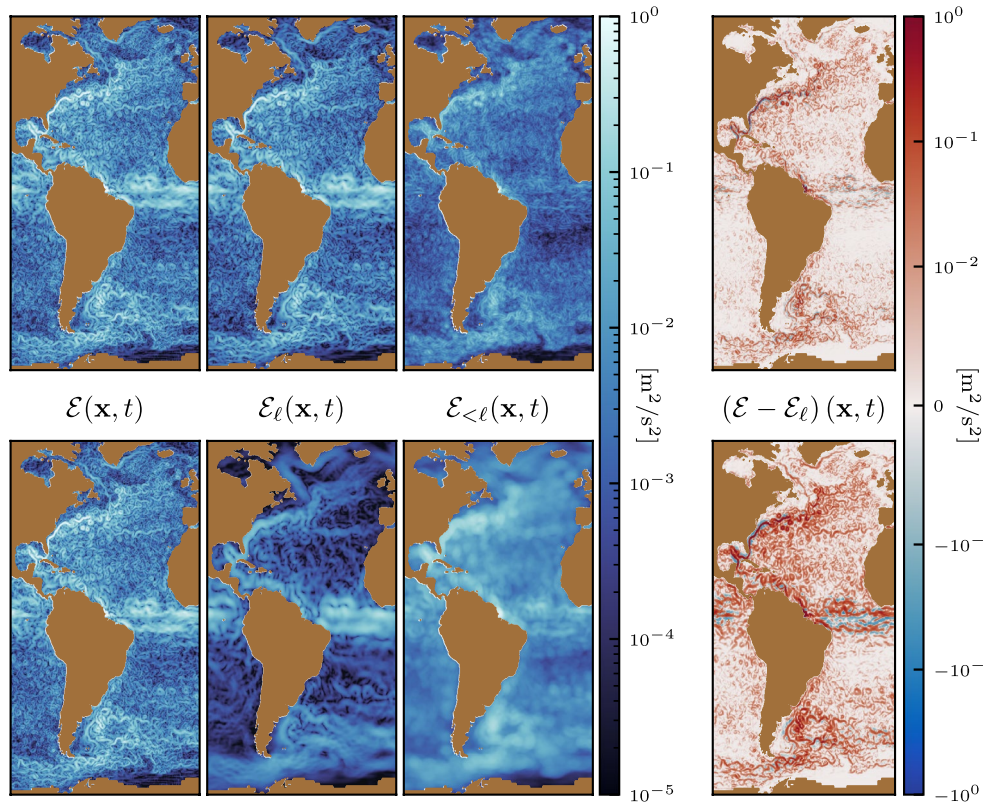

Figure 5. Maps of the coarse-grained decomposition of kinetic energy (KE) from a single day of the AVISO analysis at two different filter scales, $\ell = 100$ km (top) and $\ell = 400$ km (bottom). Here the bare KE, $\mathcal{E}(\mathbf{x},t)$, is compared with coarse KE, $\mathcal{E}_\ell(\mathbf{x},t)$, and fine KE, $\mathcal{E}_{<\ell}(\mathbf{x},t)$. The right-most column shows the fine scale term defined by Equation 20, which can yield negative values.

to both terms in Equation 10 defining $\mathcal{E}_{<\ell}$. This definition ensures that $\mathcal{E}_{<\ell}$ is positive semi-definite at each point in space and time.

Visualization of fine KE, $\mathcal{E}_{<\ell}$, is still useful to identify the regions where structures smaller than the filter scale are dominant in the ocean. Even so, one may wish to view the alternative quantity

$$\mathcal{E} - \mathcal{E}_\ell = \frac{1}{2}\left(|\mathbf{u}(\mathbf{x},t)|^2 - \left|\overline{\mathbf{u}}_\ell(\mathbf{x},t)\right|^2\right), \tag{20}$$

which is shown in the right-most column of Figure 5. This quantity reveals more fine scale features since only the second term on the right hand side is filtered. However, as discussed in Section 3.1, the energy difference, $\mathcal{E} - \mathcal{E}_\ell$, can be negative locally in space, and so it does not serve our purposes for decomposing the energy into non-negative terms.

4.2. Reynolds Averaging Decomposition

Here, and in subsequent subsections, we show that the time-mean flow consists of an entire range of length scales with substantial contributions from the mesoscale. Figure 6 shows the mean-fluctuation decomposition following the RA approach. The maps are focused on the Atlantic region to help reveal details and we show just those obtained from AVISO.

The time mean is obtained by averaging the velocity over the whole time series available, spanning 9 years. From left to right we show the total energy at a single day, the time mean energy, $MKE(\mathbf{x})$, the fluctuating eddy term, $EKE(\mathbf{x}, t)$, and the cross term, $(\mathbf{u}' \cdot \langle \mathbf{u} \rangle)/2$.

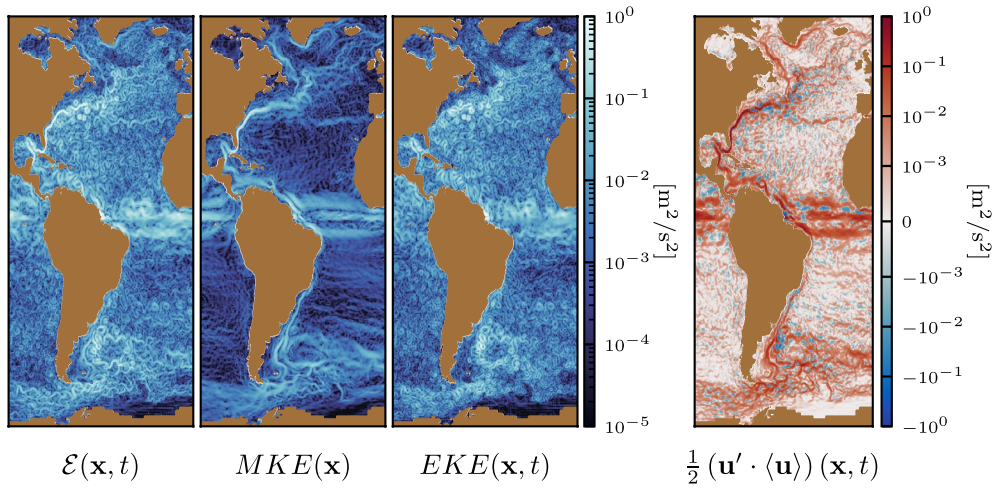

Figure 6. Decomposition of geostrophic kinetic energy from AVISO for the Atlantic basin from a time averaging (Reynolds) decomposition. Left panel: total energy, $\mathcal{E}(\mathbf{x}, t)$ at a single day. Left middle panel: 9-year time mean, $MKE(\mathbf{x})$. Right middle panel: fluctuating eddy term, $EKE(\mathbf{x}, t)$. Right panel: the cross term required to recover the total geostrophic energy as defined in Equation 18.

Having used a relatively long time series for averaging, the mean energy in Figure 6 is rather depleted away from major current systems, so that the Gulf Stream and the Antarctic Circumpolar Current are quite pronounced relative to the gyre interiors. We appreciate from this figure that the mean flow retains a substantial contribution from structures with a variety of sizes. In the same way, the "eddy" (or temporally fluctuating) flow in Figure 6 contains most of the small scale fluctuations but also a substantial contribution from large-scale structures. The cross term shown on the right panel of Figure 6 has strong fluctuations around zero, which make its contribution almost (but not exactly) zero after a spatial-average. The blending of length scales revealed by these figures reflects the inability of time averaging to decompose the KE according to length-scales.

To further investigate the role of the three Reynolds average energy terms, Figure 7 shows their temporal variability in both hemispheres.

In the first row, we see that *EKE* constitutes a substantial portion of the total energy $\mathcal{E}$ (80%) and their temporal evolution is almost indistinguishable. Both *EKE* and $\mathcal{E}$ tend to peak during the spring-summer. The bottom row of Figure 7 shows *MKE*, which is independent of time, and the cross term, which has a zero average. These two quantities are much less energetic, with the mean term ≈20% of the total and the cross term fluctuates about its zero average without a clear seasonal signal.

4.3. The Filtering Spectrum

In Figure 8 we show the cumulative large-scale energy for the north and south hemispheres as obtained from Equation 12 for AVISO and NEMO, as well as the filtering spectra for the Reynolds-decomposed components of NEMO: full time signal, $\mathcal{E}(\mathbf{x}, t)$, time mean, $MKE(\mathbf{x})$, and time varying, $EKE(\mathbf{x}, t)$. In the top panel we show the cumulative area-averaged energy spectra, $\mathcal{E}_\ell$, as a function of coarse-graining scale. In the center and bottom panels, we show the filtering spectrum (cf. Equation 12), in lin-log and log-log scale respectively.

4.3.1. Cumulative Energy Spectra

At the large k_ℓ (small ℓ) end of the cumulative spectra, we see that all four datasets converge. That is, for both NEMO and AVISO, the area-averaged energy density is $\approx 2 \times 10^{-2}$ m^2/s^2 (corresponding to an RMS velocity of ≈20 cm/s), for either hemisphere. At gyre-scales, SH has noticeably higher energy density than NH. This asymmetry is balanced by an opposing asymmetry over the mesoscales, where NH has higher KE density, which is more readily detectable in the filtering spectra. The NH-SH asymmetry can be attributed to basin geometry and continental boundaries. The NH ocean basins are land-constrained relative to the SH, which has more room for a larger-scale flow, namely the ACC, to develop and intensify. We shall see in Table 1 below that most of the hemispheric asymmetry resides in the stationary time-mean flow. The stronger (energy-per-area) mesos-

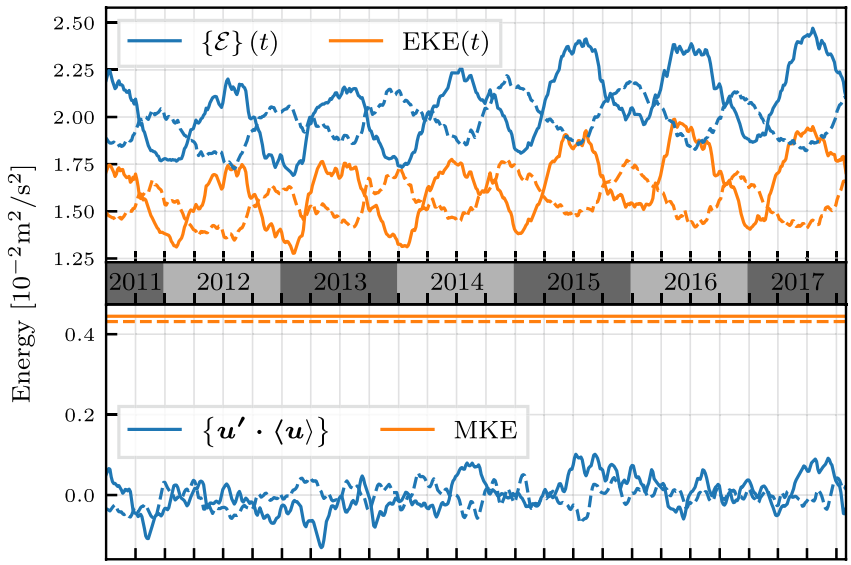

Figure 7. Top panel: Time-series of total geostrophic kinetic energy (KE), $\{\mathcal{E}(\mathbf{x})\}(t)$ (blue), and the fluctuating component, $\{EKE(\mathbf{x})\}(t)$ (orange), in the North (solid line) and South (dashed line) from the AVISO analysis. Vertical grid lines indicate the start of each quarter-year (01Jan, 01Apr, 01Jul, 01Oct). Bottom panel: Time-series of the cross term (blue) and KE of the 9-year mean, $\{MKE(\mathbf{x})\}$ (orange), in the North (solid line) and South (dashed line). *EKE* constitutes a substantial portion of the total energy and with an almost indistinguishable temporal variation. Here, we show only 6.5 years of the full 9-year record. Plots shown use a 4-day sampling frequency, but averages are based on a 1-day sampling of the 9-year record.

cale flow in the NH is stationary and is most probably due to the time-invariant forcing exerted by continental boundaries. This can explain our observation in Figure 8 (middle panel) that NH mesoscales are more intense than in the SH.

4.3.2. Filtering Spectra

The full time filtering spectra in Figure 8 have been previously reported in Storer et al. (2022). Here, we extend previous results by incorporating CG spectra of the time-mean and time-varying RA components. As might be expected, the time-mean velocity peaks spectrally at large scales ($\ell > 10^3$ km), while the time-varying component peaks over the mesoscales. This may misleadingly suggest that time-averaging produces a scale separation to a good approximation. However, as will be shown later in this subsection, the mesoscale energy (area under the spectrum plot) accounts for a majority of the time-mean energy. Therefore, as we are going to show, the time-mean flow is dominated by stationary small-scales structures <500 km in size. The length-scale at which spectra of the time-varying and time-mean velocity cross is slightly larger than 500 km.

4.3.3. Proportion of Energy in Mesoscales

In Table 1 we present the KE of the RA components partitioned at 500 km for the NEMO data set. There are three primary conclusions that can be drawn from Table 1. (a) While mesoscales are dominated by time-varying flow, the majority of the time-mean energy is also in the mesoscales. (b) The geostrophic time-varying flow is nearly entirely mesoscale, with only a few percentage points in larger scales. It is important to recall, however, that this analysis excludes ageostrophic motions, such as the Ekman flow. (c) While the full and time-varying velocities are generally consistent between hemispheres, the time-mean velocity shows strong asymmetry. Specifically, time-mean mesoscales are stronger in NH, while time-mean gyre-scales are stronger in SH. A likely contributor to the latter is the ACC. In the NH, there is stronger stationary forcing at the mesoscales relative to the SH due to more restrictive continental boundaries. Nearly identical results are found from the RA decomposition applied over the 9-year AVISO data set, shown in Appendix B.

4.3.4. RMS Velocity in Major Currents

By integrating the filtering spectrum over a scale band, we can obtain the total KE for the chosen scale band and, subsequently, the RMS velocity for that range of spatial scales. Table 2 presents these RMS velocity magnitudes from NEMO for a selection of geographic regions: NH, SH, ACC, Gulf Stream, and Kuroshio, both within the

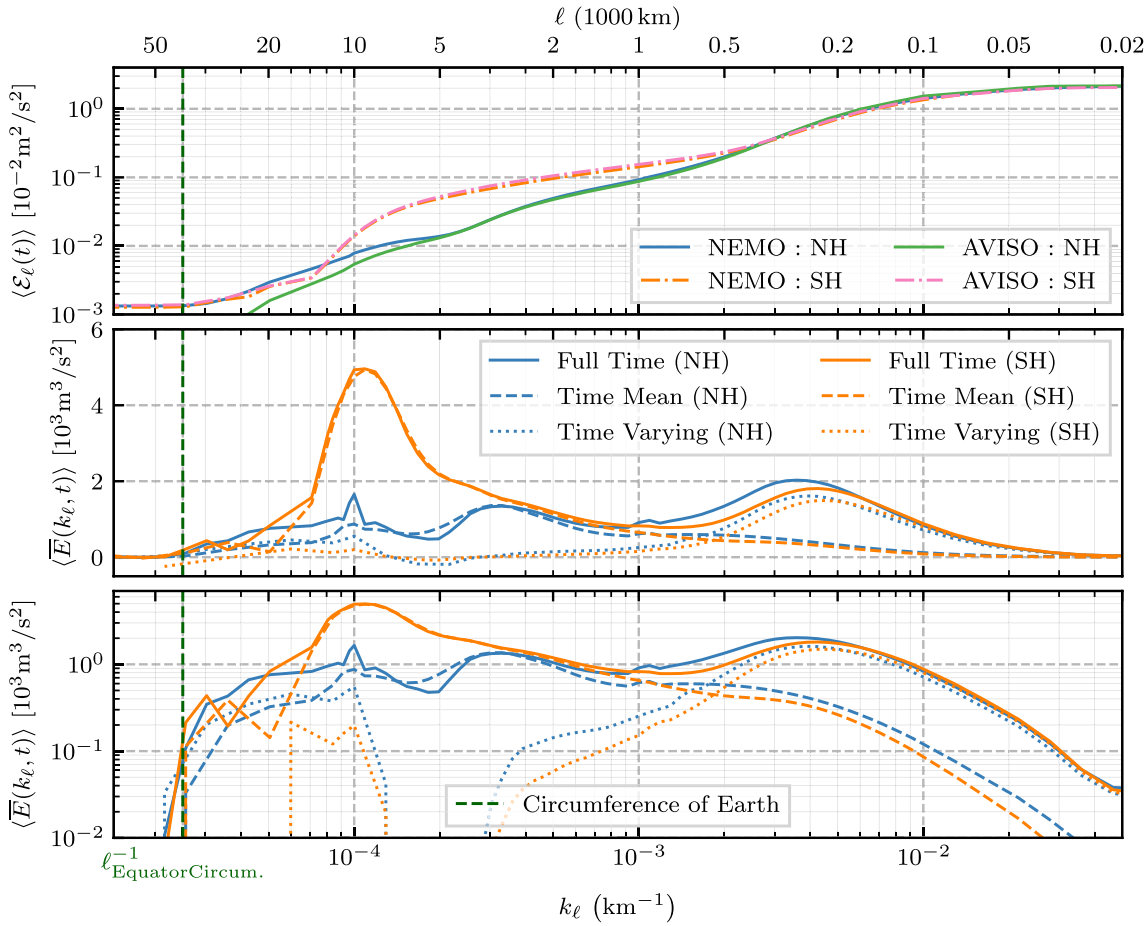

Figure 8. Power Spectra [Top]: Cumulative surface geostrophic kinetic energy spectra, $\mathcal{E}_\ell$, as a function of scale ℓ, obtained from both the AVISO and NEMO products in the North and South. [Middle and bottom]: Filtering spectra obtained following Equation 12 for the full (solid lines), time mean (dashed times), and time-varying (dotted liens) ssh-derived geostrophic velocity from the NEMO data set. Note that both middle and bottom panels show the same data, but using lin-log and log-log scales respectively.

Table 1
Mesoscale Energy for Reynolds' Components the Area-Mean Kinetic Energy Partitioned at 500 km for Each Hemisphere (Equivalent to the Top Panel of Figure 8), for the Three Reynolds' Components: Full $\mathcal{E}(\mathbf{x}, t)$, Time-Mean MKE($\mathbf{x}$), and Time-Varying Velocity EKE($\mathbf{x}$, t)

		Full Velocity	Time-Mean	Time-Varying
$\ell < 500$ km [10^{-2} m^2/s^2]	NH	2.1	0.36	1.7
	SH	2.0	0.25	1.8
$\ell > 500$ km [10^{-2} m^2/s^2]	NH	0.20	0.15	0.06
	SH	0.22	0.19	0.04
$\ell < 500$ km [% of Total]	NH	91	71	97
	SH	90	57	98

Note. Presented values are the median (50th percentile) in time from the NEMO data set. The percentages in the bottom row are the amount of energy at scales smaller than 500 km with repsect to the total energy in all scales, restricted to each hemisphere and time-component.

mesoscale (100–500 km) and gyre-scale (>10^3 km) scale-bands. The region definitions are included in Appendix C. Note that mesoscales are stronger in NH than SH, while gyre-scales are stronger in SH.

Extrapolating to Smaller Scales Both NEMO and AVISO datasets agree well on the spectral energy density of the mesoscales, down to ≈100 km, where resolution effects begin to cause deviations (Amores et al., 2018; Ballarotta et al., 2019).

Knowing the energy contained at 100 km, we can analytically integrate the total energy that would be contained below 100 km, assuming two different theoretically plausible slopes, namely k_ℓ^{-3} and $k_\ell^{-5/3}$. These power-laws are interesting because they are the theoretical predictions for the spectrum of an ideal turbulent flow in two and three dimensions respectively. Even though the ocean is far from being an ideal flow, this exercise can give a "back-of-the-envelope" estimate of the energy content of the small scales. If we let $S_{100\text{km}}$ denote the spectral energy density for $\ell = 100$ km, and assume a spectral scaling of $k^{-\alpha}$ spanning all scales smaller than 100 km, then we can compute the total amount of energy in scales smaller than 100 km as

Table 2
RMS Current Speed [cm/s] in Select Regions the Area-Mean RMS Velocity Magnitude [cm/s] for Selected Regions Using Both Block and KE-Masked Definitions, See Appendix C

	Mesoscales (100–500 km)		Gyre-scales (>10^3 km)	
Region	Block region	KE masked	Block region	KE masked
South of Tropics	15.0	—	5.3	—
ACC	16.4	28.1	7.0	9.7
North of Tropics	15.5	—	4.3	—
Gulf Stream	32.7	42.2	7.8	8.7
Kuroshio	26.5	40.0	8.1	10.1

Note. Note that there is no KE-masked variant of the NH and SH regions. Reported values are for the time median (50th percentile). Presented values are from the NEMO data set, and are all rounded to one decimal point.

$$\lim_{n\to\infty}\int_{k_\ell=10^{-5}}^{10^n} S_{100\mathrm{km}}10^{-5\alpha}k^{-\alpha}\mathrm{d}k = \frac{1}{\alpha-1}S_{100\mathrm{km}}10^{-5}, \tag{21}$$

or, alternatively, to only consider the decade spanning 10–100 km,

$$\int_{k_\ell=10^{-5}}^{10^{-4}} S_{100\mathrm{km}}10^{-5\alpha}k^{-\alpha}\mathrm{d}k = \frac{1}{\alpha-1}S_{100\mathrm{km}}10^{-5}\left[1-10^{1-\alpha}\right], \tag{22}$$

where we assume that $\alpha > 1$. Using Equations 21 and 22 and the 100 km values presented in Figure 8, we can then compute the amount of energy in scales smaller than 100 km as a percentage of energy *across all scales*. These values are presented in Table 3 and reveal that as much as 25%–50% of the surface geostrophic KE is contained in scales smaller than 100 km. These scales are un(der)-resolved by pre-SWOT satellite products. Our estimates are contingent on a persistent power-law scaling over small scales, but they nevertheless illustrate how a substantial proportion of surface geostrophic energy may be missed by coarse resolution.

4.3.5. Zonally-Averaged Coarse Energy

In Figure 9 we plot the zonally-averaged KE for selected length-scale bands. Scales larger than 10^3 km (blue plot in Figure 9) have a dominant contribution from latitudes [60°S, 40°S], which roughly corresponds with the ACC. However, these latitudes are no longer dominant when considering the band of smaller scales: 215 km $< \ell <$ 10^3 km. These scales (orange plot in Figure 9) show a distinct signal at latitudes [30°N, 40°N], which roughly aligns with the Gulf Stream and Kuroshio. There is also a weaker signal at latitudes [40°S, 35°S], which roughly aligns with the Agulhas and the Brazil-Malvinas currents.

4.4. Spatio-Temporal Decomposition

In this section, we present results from coarse-graining in both space and time to reveal all the length-scales present in the time-averaged currents up to 9-year temporal mean. Our analysis demonstrates a way for comparing data from satellite analysis (AVISO) and numerical models (NEMO).

The approach consists of measuring the filtering spectrum of a temporally-smoothed version of the original velocity field. The latter is obtained from a running window time average,

$$\langle\mathbf{u}\rangle_\tau(\mathbf{x},t) = \frac{1}{\tau}\int_{t-\tau/2}^{t+\tau/2}\mathbf{u}\left(\mathbf{x},t'\right)\,\mathrm{d}t', \tag{23}$$

with τ the size of the time window. Note that a running window time-average in Equation 23 is similar to spatial coarse-graining (Equation 1) since

$$\langle\langle F\rangle_\tau\rangle_\tau \neq \langle F\rangle_\tau. \tag{24}$$

Combining Equation 12 with Equation 23 allows us to measure the filtering energy spectrum of the time-smoothed field

$$\overline{E}(k_\ell,\tau) = \left\langle \frac{d}{dk_\ell}\left\{\frac{1}{2}\left|\langle\overline{\mathbf{u}}_\ell\rangle_\tau\right|^2\right\}\right\rangle = \left\langle\frac{d}{dk_\ell}\{\mathcal{E}_{\ell,\tau}\}\right\rangle, \tag{25}$$

where we introduced

$$\mathcal{E}_{\ell,\tau}(\mathbf{x},t) = \frac{1}{2}\left|\left\langle\overline{\mathbf{u}}_\ell\right\rangle_\tau\right|^2, \tag{26}$$

Table 3
Extrapolated Small-Scale Energy Percentage of Total Kinetic Energy Integrating Scales in the Decade Spanning 10–100 km

	AVISO		NEMO	
$-\alpha$	NH	SH	NH	SH
−3	24% [24%]	25% [25%]	23% [23%]	25% [25%]
−5/3	43% [49%]	44% [50%]	41% [47%]	44% [50%]

Note. Values in brackets ([·]) arise from integrating all scales smaller than 100 km assuming a constant power-law scaling of $k^{-\alpha}$.

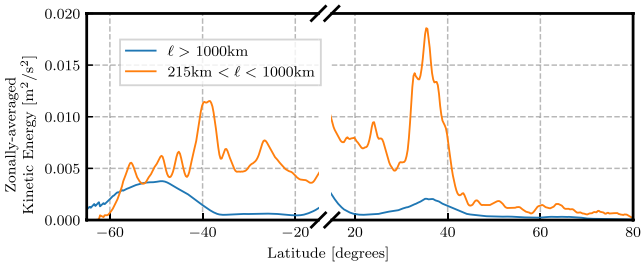

Figure 9. Time- and zonally-averaged kinetic energy computed from AVISO within selected length-scale bands (see in-set legend) as a function of latitude. We can see that the Antarctic Circumpolar Current has significant energy at scales $>10^3$ km, while the North has significant energy within ≈30°N–40°N where the Western Boundary Currents are located. Note that the latitude axis is broken to exclude the band [15°S, 15°N].

which is the cumulative spectrum of the temporally-smoothed field. As indicated, $\mathcal{E}_{\ell,\tau}(\mathbf{x},t)$ is a function of both the size of the time window, τ, and the spatial kernel, ℓ.

Time-Averaged Spatial Maps We show the time-smoothed energy map, $\mathcal{E}_{\ell=0,\tau}$, in Figure 10 from AVISO. Here, the two columns compare results from the North and the South regions, while different rows compare results with different time windows, τ. From these maps we can see that increasing τ from 1 day to 1,093 days reduces the energy down to ≈21% (≈25%) of the original total energy in the North (South). Hence, averaging over 3 years brings the energy down to values comparable to those over the full 9 years obtained in the previous section by the RA decomposition, where we found that *MKE* accounts for ≈20% of the total energy in the extra-tropics. This result indicates that temporal averaging converges quickly for the geostrophic KE, and using longer time records does not significantly alter the partitioning between the temporal mean and fluctuating components of the surface geostrophic ocean flow.

4.5. Spatio-Temporal Comparison of AVISO and NEMO

We now demonstrate using a spatio-temporal coarse-graining, which may complement current efforts to disentangle balanced from unbalanced motions in SSH-derived flows. Figure 11 presents space-time 2-D spectra, $-\langle \frac{d}{d\tau}\frac{d}{dk_\ell}\{\mathcal{E}_{\ell,\tau}\}\rangle$, which decomposes the energy as measured from AVISO and NEMO. In the left (right) column of Figure 11 we show the isolevels of space-time spectra from NEMO (AVISO). Note that the NEMO spectra extend to smaller length scales due to having higher spatial resolution, but that the panels have consistent spacing/aspect ratios. The most pronounced difference is that the AVISO isocontours are more circular, while NEMO isocontours or more elongated and tilted, hinting at an $\ell - \tau$ relationship. In both datasets, energy peaks at approximately $\ell = 200$ km and $\tau = 2 - 3$ weeks.

Time-averaging to Align Spectra Remember that for the entire analysis in this paper, we are using 1-day averages of SSH to derive velocity from the NEMO data. While the SSH from AVISO is also available daily, it is effectively averaged over longer periods of time to produce gridded SSH maps from along-track altimeter data. We propose that the difference between isocontours from AVISO and NEMO in Figure 11 comes from the optimal interpolation used to produce the gridded AVISO product (Pujol et al., 2016), which is necessary to construct the global maps from satellite altimeters' along-track data. To support this hypothesis, in Figure 12 we show the

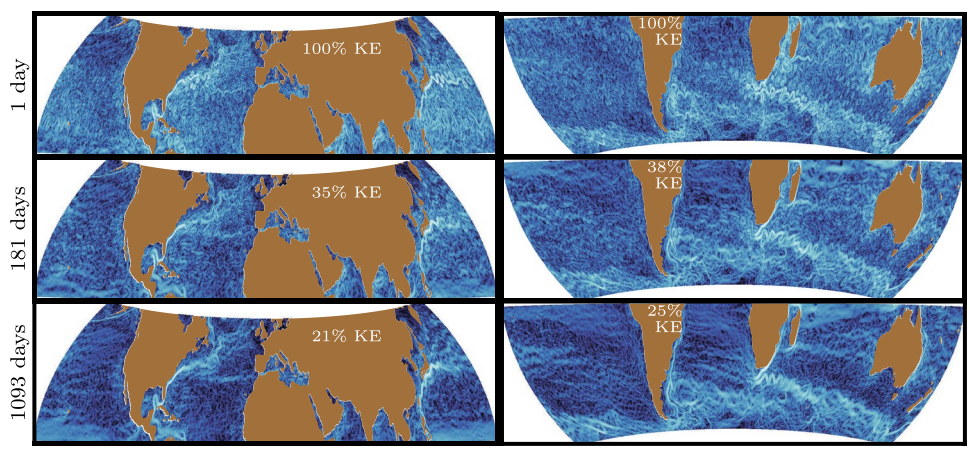

Figure 10. The surface geostrophic kinetic energy (KE) from the temporally coarse-grained flow, $\mathcal{E}_{\ell=0,\tau}$, in the North (left column) and South (right column) from AVISO. The top row shows the original 1-day averaged flow. The middle and bottom rows show the KE from the flow when averaged with a ≈6 months time window and a ≈3 years time window, respectively, with the KE decreasing with an increasing time window. Each panel indicates the % of KE remaining relative to the 1-day top row.

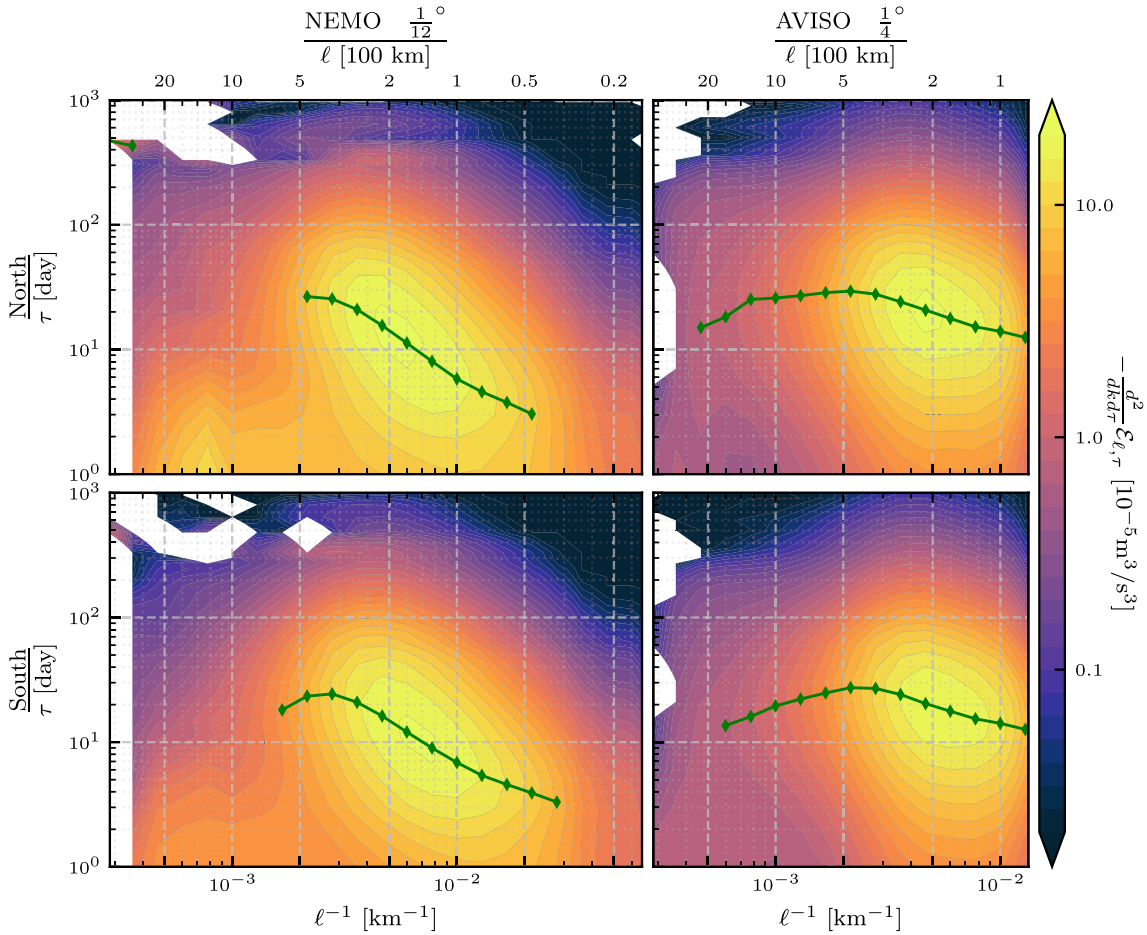

Figure 11. Combined spatio-temporal coarse-graining producing 2D spectra, $-\partial_\tau \partial_{k_\ell} \mathcal{E}_{\ell,\tau}$ from [left] 1/12° NEMO and [right] AVISO, averaged over the [top] NH and [bottom] SH. Mesoscale energy predominantly peaks on length-scales of 100–200 km and time-scales of 1–3 weeks. Green diamonds indicate, for each ℓ, the τ at which spectral power is maximized (cf. Figure 13).

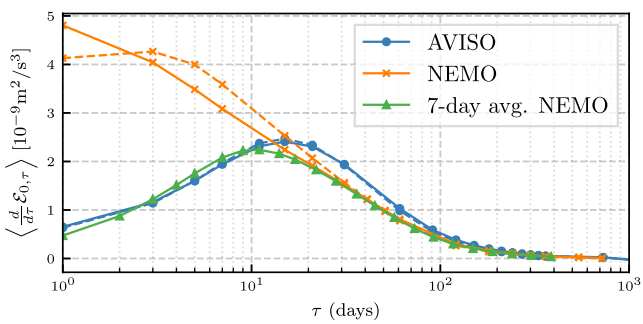

Figure 12. Evidence that the disagreement between AVISO and NEMO over time-scales $\lesssim$10 days is due to temporal averaging used in generating the gridded AVISO product. Here, we show temporal spectra from AVISO (blue) and NEMO (red) in the North (solid lines) and South (dashed lines), which disagree over $\tau \lesssim 10$ days as in Figure 11. However, the temporal spectra from NEMO agree with those from AVISO after applying a 7-day temporal smoothing to the original NEMO velocities (green). This result supports our hypothesis that AVISO is missing dynamical information at time-scales less than 10 days due to temporal smoothing over all length-scales.

spectra as a function of τ measured from AVISO and NEMO. In this plot, we have repeated the analysis of the NEMO spectra after passing the data through a 7-day running time average (green line), which reproduces the time average over the satellite orbits. We can see that the green curve overlaps the AVISO measurement (blue) very closely, supporting our hypothesis. This is similar to what was observed in Biri et al. (2016); Chassignet and Xu (2017) who performed a similar exercise on the AVISO altimeter spectrum and also in what was found in Arbic et al. (2014); Khatri et al. (2018); Renault et al. (2019) who compared the cascade of AVISO and model data and determined that AVISO's spectral fluxes can be reproduced from model data after filtering the latter in both space and time.

Possible Role of Unbalanced Motions What component of the flow could be yielding the discrepancy between NEMO and AVISO? The most obvious possibility is unbalanced motion present in the 1-day mean SSH fields of NEMO that is absent from AVISO due to the effective weekly averaging required for gridding the satellite measurements. However, unbalanced motion had been believed to be important mostly over length-scales $\lesssim$100 km and time-scales $\lesssim$2 days (e.g., Richman et al., 2012; Qiu et al., 2018). If our conjecture is correct, it would imply that unbalanced motion is present at all scales between 200 km to 10^3 km, with significant differences even between

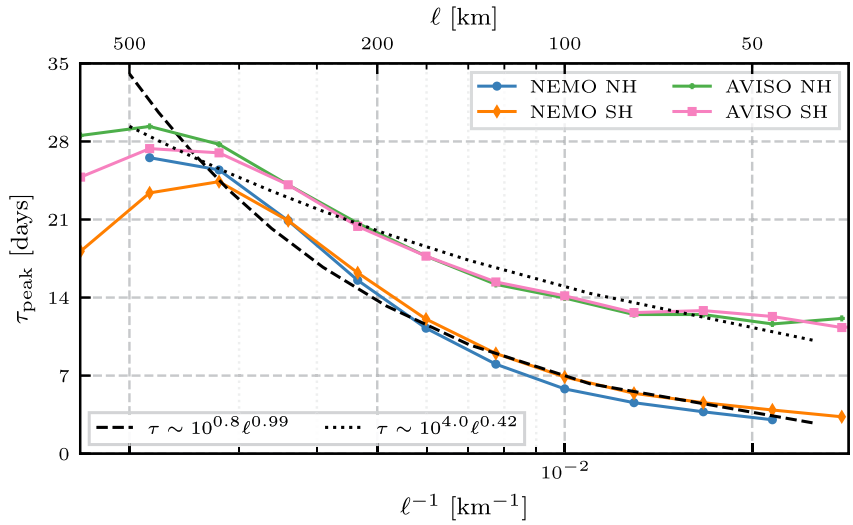

Figure 13. Mesoscale τ-ℓ Relationship For each filter scale (ℓ), the time-scale (τ_{peak}) for which the power spectrum $\left(-\partial_\tau \partial_{k_\ell} \mathcal{E}_{\ell,\tau}\right)$ is maximized. While dashed lines show regression fits (see legend for regression formulas), which express τ [s] in terms of ℓ [m].

1–2 $\times$ 10^3 km and $\tau \approx$ 1–10 days as shown in Figure 11, requiring averaging over a few days to be removed. Isolating balanced from unbalanced motions (e.g., Bühler et al., 2014) is an active research topic that is beyond the scope of this work. Another possible explanation can be found in the time-smoothing of balanced motions, which is inherent in the construction of the AVISO data set. Indeed in (Arbic et al., 2013, 2014) they removed high-frequency motions with a 3-day low-pass filter before applying spectral analysis and they obtained similar results as the ones we observed here.

4.5.1. Relating Time-Scale to Length-Scale

As discussed, Figure 11 shows a clear mesoscale spectral structure centered roughly on 200 km and 14 days. In Figure 13 we present for each spatial scale ℓ, the time-scale τ for which $-\partial_\tau \partial_{k_\ell} \mathcal{E}_{\ell,\tau}$ is maximized. We use cubic interpolation in the τ-dimension to compensate for only having data points for an odd integer number of days. These results are broadly similar between hemispheres, however, there are noticeable disagreements between NEMO and AVISO. The two agree on the time scale of the largest mesoscales (400–500 km), with AVISO consistently yielding longer time scales than NEMO for smaller ℓ. NEMO presents $\tau \sim \ell$ over the mesoscale band, while AVISO gives $\tau \sim \ell^{0.4}$.

4.5.2. Connection to Space-Time Spectra in the Literature

Figure 11 shows the importance of performing a combined spatio-temporal decomposition to access all information in the data. Our method is similar to frequency-wavenumber analysis performed within Fourier boxes by several recent studies: Arbic et al. (2014) were interested in mesoscale-driven intrinsic low-frequency variability, while Savage et al. (2017); Qiu et al. (2018); Torres et al. (2018) were primarily motivated by isolating the unbalanced motions from SSH-derived velocities. Our Figure 11 is analogous, for example, to Figure 4 in Arbic et al. (2014) and to Figure 3 in Torres et al. (2018), although the latter analyzed higher frequencies than those that are available in the datasets that we study here. It is important to stress that high-frequency forcing was not employed in the production of the NEMO model data used in our work and high-frequency motions are not our current focus of interest, while the latter works employed models with simultaneous atmospheric and tidal forcing which entails the formation of an internal gravity wave continuum spectrum as first described in Muller and Bony (2015), Rocha et al. (2016). However, as we mentioned in the introduction, the coarse-graining approach gives us access to the *global* energy budget and, moreover, frees us from the limitations of Fourier boxes and the required tapering and detrending. As such, the approach here complements previous frequency-wavenumber analysis by allowing us to access much larger length-scales.

A common feature between our Figure 11 and those in previous studies is a slight elongation of isocontours along the diagonal from small to large spatio-temporal scales in the main panel of our Figure 11. Such elongation is

most prominent in Figure 3 of Torres et al. (2018), who were probing scales <100 km and from roughly 3 hr to 40 days. The diagonal elongation of isocontours represents a slight tendency for larger length-scales to have longer time-scales.

However, we emphasize that unlike in Torres et al. (2018), such tendency is only *slight* over the larger scales we analyze here. In fact, an important take-away from Figure 11 is that all length-scales evolve over a wide range of time-scales. Consider, for example, $\ell \approx 500$ km in the left column of Figure 11 at different τ values. We see that the isoline is almost vertical over $\tau \approx 5$ days to $\tau \approx 50$ days, indicating that flow at 500 km has an equal contribution from all these time-scales. We also see that both AVISO and NEMO isolines get flatter (stretched horizontally) as τ increases, such that at $\tau \approx 300$ days, there is almost equal energy at all scales between ≈100 km and $\approx 10^3$ km.

5. Conclusions

5.1. Summary of the Main Results

In this paper we expanded on a recent calculation of the first global energy spectrum of the ocean's surface geostrophic circulation (Storer et al., 2022) using the coarse-graining (CG) method. Our analysis here gives new insights into the oceanic circulation. The method is implemented in an open-source software, FlowSieve (Storer & Aluie, 2023), that can be accessed at https://github.com/husseinaluie/FlowSieve.

In this work, we compare quantitatively the CG and the spherical harmonics decompositions. While the two methods yield qualitatively consistent domain-averaged results, spherical harmonics spectra are too noisy at gyre scales. More importantly, spherical harmonics are inherently global and cannot provide local information connecting scales with currents geographically.

We have estimated that the RMS velocity of the mesoscales is globally around 15 cm/s, but it increases up to 30–40 cm/s in the Kuroshio or the Gulf Stream and up to 16–28 cm/s in the ACC. We find notable hemispheric asymmetry in mesoscale energy-per-area, which is higher in the north, bringing to the fore the significance of domain geometry. Indeed, mesoscales can arise from boundary forcing, which is coherent in time and is distinct from the baroclinic instability often discussed as the main driver of mesoscales.

In this paper, we applied the coarse-graining approach to the Reynolds decomposed fields, namely the time-mean and the time-varying terms of the ocean surface currents. Results in this direction highlight that while the time-varying term is largely dominated by the mesoscales, (≈98%), the time-mean component also has a majority (up to 70%) contribution from the mesoscale circulation. This highlights the preponderance of "standing" small-scale structures in the global ocean and the potentially significant role played by forcing from the ocean boundaries, which is temporally coherent. It also shows that Reynolds decomposition is an ineffective method for disentangling eddy structures from the flow.

By coarse-graining in both space and time, we have shown that every length-scale evolves over a wide range of time-scales. This result makes us appreciate the significance of temporally coherent (even stationary) forcing mechanisms acting on the mesoscales, such as bottom topography and continental boundaries. An important new contribution of this work is the spatio-temporal spectra of the geostrophic currents. These 2D spectra highlight how the mesoscales while peaking at ≈(200 km, 2 weeks), are not only diffused over a range of spatial scales, but also vary over a wide range of temporal scales. Further, we extract the dominant time-scale, τ_{peak} for each filter scale in the mesoscale band, and find that NEMO predicts $\tau \sim \ell$, which leads to a length scale-independent advective velocity of 0.15–0.2 cm/s. In contrast, AVISO demonstrates consistently longer dominant time-scales, and a shallower relationship of $\tau \sim \ell^{0.4}$, both of which are likely results of the time averaging needed to extract the AVISO velocity maps.

5.2. Coarse-Graining and the Filtering Spectrum

The coupling between different length- and time-scales and between different geographic regions presents a major difficulty in understanding, modeling, and predicting oceanic circulation and mixing. Indeed, the oceanic KE budget is estimated to suffer from large uncertainties (Ferrari & Wunsch, 2009). A major reason behind these difficulties is a lack of scale-analysis methods that are appropriate in the *global* ocean. In this paper,

we have demonstrated the versatility of coarse-graining in serving as a robust scale-analysis method for the global ocean circulation that complements existing methods. The approach is very general, allows for probing the dynamics simultaneously in scale and in space, and is not restricted by assumptions of homogeneity or isotropy commonly required for traditional methods such as Fourier or structure-function analysis. We note that coarse-graining includes wavelet analysis (Uchida et al., 2023) as a special case with the proper choice of convolution kernel, which disentangles the flow from a band of scales instead of partitioning it into large-scales and small-scales (Sadek & Aluie, 2018). Coarse-graining offers a way to probe and quantify the energy budget at different length-scales globally while maintaining local information about the heterogeneous oceanic regions. We view this work as an important step toward constructing a scale-aware global Lorenz Energy Cycle for the ocean circulation (Loose et al., 2023).

Appendix A: Deforming the Kernel Around Land

As outlined in Section 3.1, filtering with a constant kernel while treating land as zero-velocity water and including land cells ("Fixed Kernel w/Land") in the final tally is guaranteed to conserve 100% of the energy, while excluding land cells and integrating only over water cells ("Fixed Kernel w/o Land") leads to a loss of about 11% of the total KE at a filter scale of 2,000 km (see Figure 2). This result follows since some of the KE "smears" onto the land cells, which are then excluded from the spatial integrals.

An alternative approach is to deform the kernel around land ("Deforming Kernel") so that only water cells are incorporated in the filtering operation. This approach has the advantage of not needing to treat land as water, yet we have shown in Figure 2 that this choice still does not conserve 100% of the energy, sometimes even yielding larger values, albeit still within 1% error. Here, we explain why a deforming a kernel cannot be expected to yield 100% of the energy, unlike the "Fixed Kernel w/Land."

To illustrate how the loss of energy conservation can happen with the Deforming Kernel method, consider a one-dimensional domain with five equally spaced points and a simple kernel that has a weight of 2 at the target point, 1 at neighboring points, and 0 otherwise.

If the domain were periodic then the filtering operation could be represented as the matrix

$$G := \begin{bmatrix} 1/2 & 1/4 & 0 & 0 & 1/4 \\ 1/4 & 1/2 & 1/4 & 0 & 0 \\ 0 & 1/4 & 1/2 & 1/4 & 0 \\ 0 & 0 & 1/4 & 1/2 & 1/4 \\ 1/4 & 0 & 0 & 1/4 & 1/2 \end{bmatrix} \tag{A1}$$

such that $\overline{\mathrm{KE}} = G \cdot \mathrm{KE}$, where KE is a column vector. Note that the sum of each row of G is 1, a result of normalizing the kernel (assuming a grid spacing of 1 for simplicity). Domain integrating in this scenario is simply left-multiplying by the row vector S:=[1, 1, 1, 1, 1], which is equivalent to taking a column-wise sum. Since $S \cdot G = S$, $S \cdot \overline{\mathrm{KE}} = S \cdot G \cdot \mathrm{KE} = S \cdot \mathrm{KE}$, and so the domain-integrated KE is conserved.

However, if the domain is non-periodic (such as if the edges were "land"), then the deforming kernel that excludes anything outside the boundaries would be

$$G := \begin{bmatrix} 2/3 & 1/3 & 0 & 0 & 0 \\ 1/4 & 1/2 & 1/4 & 0 & 0 \\ 0 & 1/4 & 1/2 & 1/4 & 0 \\ 0 & 0 & 1/4 & 1/2 & 1/4 \\ 0 & 0 & 0 & 1/3 & 2/3 \end{bmatrix} \tag{A2}$$

In this case, $S \cdot G = [11/12, 13/12, 1, 13/12, 11/13] \neq S$, and so in general $S \cdot \overline{\mathrm{KE}} \neq S \cdot \mathrm{KE}$. Moreover, there is no guarantee that $S \cdot \overline{\mathrm{KE}} \leq S \cdot \mathrm{KE}$, and so it may be that the total filtered KE exceeds the total unfiltered KE.

As observed, in general, the error arising from deforming the kernel will be much smaller than that of treating land as zero-velocity water and only integrating over true water cells, especially for large filter kernels. However, again, it is worth recognizing that deforming the kernel does not guarantee energy conservation. To fully conserve energy and maintain commutativity with differentiation, we choose the "Fixed Kernel w/Land" option, which treats land as zero-velocity water and includes land cells in spatial integrals to compute total energy.

Appendix B: Reynolds Averaging Spectra on AVISO Dataset

Figure B1 reports the energy spectra for the time-mean and time-varying RA components obtained from the 9-year AVISO data set. Results are in very good agreement with the spectra obtained from NEMO data set, presented in Figure 8. The values obtained from the two datasets are nearly identical, with the AVISO data set having less small-scale energy owing to having a lower resolution.

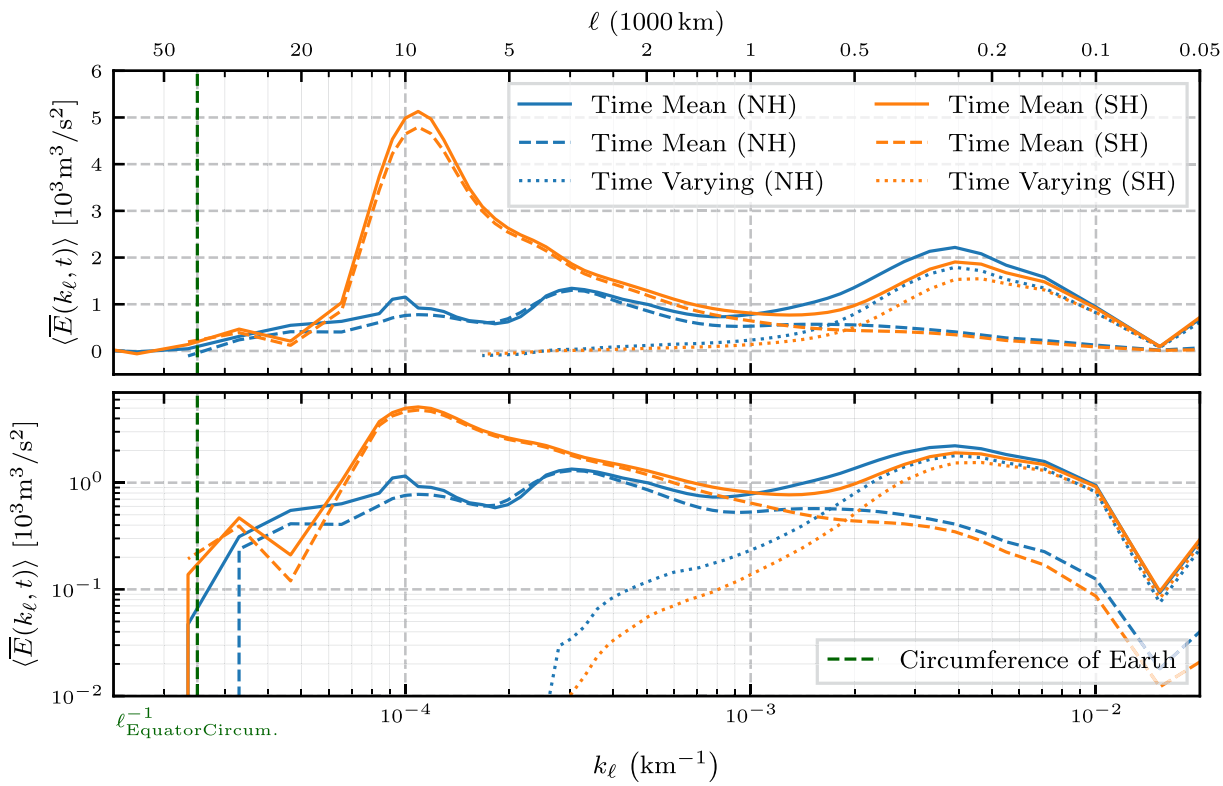

Figure B1. Power Spectra Filtering spectra obtained following Equation 12 for the full (solid lines), time mean (dashed times), and time-varying (dotted liens) ssh-derived geostrophic velocity from the AVISO data set. Note that both top and bottom panels show the same data, but using lin-log and log-log scales respectively.

Appendix C: Geographic Definitions for Current Regions

Equations C2–C6 outline the geographic constraints used to define the various regions used in Table 2. In each definition, λ is longitude in degrees, ranging from -180 to 180, and ϕ is latitude in degrees, ranging from -90 to 90. Additionally, any overlap with land is removed from the region definition, so that only water cells are included. The region masks are presented in Figure C1.

Energy Masking Following Rai et al. (2021), subsets of the regions defined in Equations C2–C6 are produced by further restricting to areas with sufficiently high "masking KE." For these purposes, a combination of time-mean and time-varying KE is used such that

$$\text{Masking KE} = \frac{1}{2}\rho_0\langle \mathbf{u}\rangle^2 + \frac{1}{2}\rho_0\left\langle (\mathbf{u} - \langle \mathbf{u}\rangle)^2\right\rangle. \tag{C1}$$

Taking $\rho_0 = 1{,}025$, a cut-off of Masking KE > 50 is applied to the Gulf Stream and Kuroshio, and Masking KE > 30 to the ACC. The KE-masked regions are illustrated with dots in Figure C1.

$$\textbf{North of Tropics}: \quad \phi > 15^\circ \tag{C2}$$

$$\begin{aligned}\textbf{Kuroshio}: \quad & \{120^\circ < \lambda < 170^\circ\} \\ & \text{and } \{17^\circ < \phi < 45^\circ\} \\ & \text{and } \{\phi \le (3/4)\lambda - 60^\circ\} \\ & \text{and } \{\text{not } (\phi < 25^\circ \text{ and } \lambda \ge 140^\circ)\} \\ & \text{and } \{\text{not } (\lambda \le 140^\circ \text{ and } \phi < (2/5)\lambda - 31^\circ)\}\end{aligned} \tag{C3}$$

$$\textbf{Gulf Stream}: \quad \{-80.75^\circ < \lambda < -35^\circ\} \text{ and } \{|\phi - (2/5)\lambda - 62^\circ| \le 6^\circ\} \tag{C4}$$

$$\textbf{South of Tropics}: \quad \phi < -15^\circ \tag{C5}$$

$$\begin{aligned}\textbf{ACC}: \quad & \{-70^\circ < \phi < -33^\circ\} \\ & \text{and } \{\text{not } (\lambda < -72^\circ) \text{ and } \phi > -(5/108)\lambda - 160/3^\circ\} \\ & \text{and } \{\text{not } (\lambda > 20^\circ) \text{ and } \phi > -(3/40)\lambda - 63/2^\circ\}\end{aligned} \tag{C6}$$

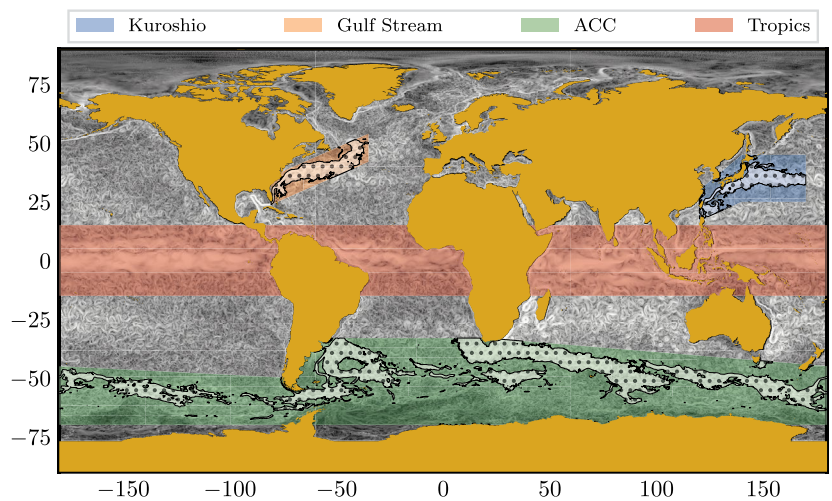

Figure C1. Illustration of the geographic region definitions (Equations C2–C6), plotted over a sample velocity field for reference. Note that "North of Tropics" and "South of Tropics" are not included, but are simply the portions North and South of "Tropics." For "Kuroshio," "Gulf Stream," and "ACC," the smaller contoured region with dots shows the region definition with an additional kinetic energy mask.

Data Availability Statement

This study has been conducted using E.U. Copernicus Marine Service Information. The product identifier of the AVISO dataset used in this work is (AVISO, 2021), and can be downloaded at https://marine.copernicus.eu/services-portfolio/access-to-products/. The product identifier of the NEMO dataset is (NEMO, 2021), and is available at https://marine.copernicus.eu/services-portfolio/access-to-products/. The source code for the coarse-graining software FlowSieve (Storer & Aluie, 2023) has been archived on Zenodo [https://doi.org/10.5281/zenodo.7818192, URL: https://doi.org/10.5281/zenodo.7818192].

Acknowledgments
We thank B. Reichl, D. Balwada, M. Jansen, and S. Rai for their valuable discussions and comments. We also thank E. Yankovsky and B. Arbic for their valuable feedback and suggestions. This research was funded by US NASA Grant 80NSSC18K0772 and NSF Grant OCE-2123496. HA was also supported by US DOE Grants DE-SC0014318, DE-SC0020229, DE-SC0019329, NSF Grants PHY-2020249, PHY-2206380, and US NNSA Grants DE-NA0003856, DE-NA0003914, DE-NA0004134. MB was also supported by the European Research Council (ERC) under the European Union's Horizon 2020 research and innovation programme (Grant Agreement No. 882340). HK was supported by UK NERC Grant NE/T013494/1. Computing time was provided by NERSC under Contract No. DE-AC02-05CH11231 and NASA's HEC Program through NCCS at Goddard Space Flight Center.

References

Aluie, H. (2013). Scale decomposition in compressible turbulence. *Physica D: Nonlinear Phenomena*, *247*(1), 54–65. https://doi.org/10.1016/j.physd.2012.12.009

Aluie, H. (2017). Coarse-grained incompressible magnetohydrodynamics: Analyzing the turbulent cascades. *New Journal of Physics*, *19*(2), 025008. https://doi.org/10.1088/1367-2630/aa5d2f

Aluie, H. (2019). Convolutions on the sphere: Commutation with differential operators. *GEM-International Journal on Geomathematics*, *10*(1), 9. https://doi.org/10.1007/s13137-019-0123-9

Aluie, H., & Eyink, G. (2009). Localness of energy cascade in hydrodynamic turbulence. II. Sharp spectral filter. *Physics of Fluids*, *21*(11), 115108. https://doi.org/10.1063/1.3266948

Aluie, H., Hecht, M., & Vallis, G. K. (2018). Mapping the energy cascade in the North Atlantic Ocean: The coarse-graining approach. *Journal of Physical Oceanography*, *48*(2), 225–244. https://doi.org/10.1175/jpo-d-17-0100.1

Aluie, H., Li, S., & Li, H. (2012). Conservative cascade of kinetic energy in compressible turbulence. *The Astrophysical Journal Letters*, *751*(2), L29. https://doi.org/10.1088/2041-8205/751/2/l29

Aluie, H., & Teeraratkul, C. (2023). Theory of large eddy simulation on the sphere. in preparation.

Amores, A., Jordà, G., Arsouze, T., & Le Sommer, J. (2018). Up to what extent can we characterize ocean eddies using present-day gridded altimetric products? *Journal of Geophysical Research: Oceans*, *123*(10), 7220–7236. https://doi.org/10.1029/2018jc014140

Arbic, B. K. (2022). Incorporating tides and internal gravity waves within global ocean general circulation models: A review. *Progress in Oceanography*, *206*, 102824. https://doi.org/10.1016/j.pocean.2022.102824

Arbic, B. K., Garner, S. T., Hallberg, R. W., & Simmons, H. L. (2004). The accuracy of surface elevations in forward global barotropic and baroclinic tide models. *Deep Sea Research Part II: Topical Studies in Oceanography*, *51*(25–26), 3069–3101. https://doi.org/10.1016/j.dsr2.2004.09.014

Arbic, B. K., Müller, M., Richman, J. G., Shriver, J. F., Morten, A. J., Scott, R. B., et al. (2014). Geostrophic turbulence in the frequency–wavenumber domain: Eddy-driven low-frequency variability. *Journal of Physical Oceanography*, *44*(8), 2050–2069. https://doi.org/10.1175/jpo-d-13-054.1

Arbic, B. K., Polzin, K. L., Scott, R. B., Richman, J. G., & Shriver, J. F. (2013). On eddy viscosity, energy cascades, and the horizontal resolution of gridded satellite altimeter products. *Journal of Physical Oceanography*, *43*(2), 283–300. https://doi.org/10.1175/jpo-d-11-0240.1

Arbic, B. K., Scott, R. B., Flierl, G. R., Morten, A. J., Richman, J. G., & Shriver, J. F. (2012). Nonlinear cascades of surface oceanic geostrophic kinetic energy in the frequency domain. *Journal of Physical Oceanography*, *42*(9), 1577–1600. https://doi.org/10.1175/jpo-d-11-0151.1

AVISO. (2021). AVISO. [Dataset]. AVISO. https://doi.org/10.48670/moi-00148

Ballarotta, M., Ubelmann, C., Pujol, M.-I., Taburet, G., Fournier, F., Legeais, J.-F., et al. (2019). On the resolutions of ocean altimetry maps. *Ocean Science*, *15*(4), 1091–1109. https://doi.org/10.5194/os-15-1091-2019

Barkan, R., Srinivasan, K., Yang, L., McWilliams, J. C., Gula, J., & Vic, C. (2021). Oceanic mesoscale eddy depletion catalyzed by internal waves. *Geophysical Research Letters*, *48*, e2021GL094376. submitted. https://doi.org/10.1002/essoar.10507068.1

Biferale, L., Bonaccorso, F., Buzzicotti, M., & Iyer, K. P. (2019). Self-similar subgrid-scale models for inertial range turbulence and accurate measurements of intermittency. *Physical Review Letters*, *123*(1), 014503. https://doi.org/10.1103/PhysRevLett.123.014503

Biri, S., Serra, N., Scharffenberg, M. G., & Stammer, D. (2016). Atlantic sea surface height and velocity spectra inferred from satellite altimetry and a hierarchy of numerical simulations. *Journal of Geophysical Research: Oceans*, *121*(6), 4157–4177. https://doi.org/10.1002/2015jc011503

Bryan, F. O., Gent, P. R., & Tomas, R. (2014). Can southern ocean eddy effects be parameterized in climate models? *Journal of Climate*, *27*(1), 411–425. https://doi.org/10.1175/jcli-d-12-00759.1

Bühler, O., Callies, J., & Ferrari, R. (2014). Wave-vortex decomposition of one-dimensional ship-track data. *Journal of Fluid Mechanics*, *756*, 1007–1026. https://doi.org/10.1017/jfm.2014.488

Busecke, J. J. M., & Abernathey, R. P. (2019). Ocean mesoscale mixing linked to climate variability. *Science Advances*, *5*(1), eaav5014. https://doi.org/10.1126/sciadv.aav5014

Buzzicotti, M., Aluie, H., Biferale, L., & Linkmann, M. (2018). Energy transfer in turbulence under rotation. *Physical Review Fluids*, *3*(3), 034802. https://doi.org/10.1103/physrevfluids.3.034802

Buzzicotti, M., & Clark Di Leoni, P. (2020). Synchronizing subgrid scale models of turbulence to data. *Physics of Fluids*, *32*(12), 125116. https://doi.org/10.1063/5.0031835

Buzzicotti, M., Linkmann, M., Aluie, H., Biferale, L., Brasseur, J., & Meneveau, C. (2018). Effect of filter type on the statistics of energy transfer between resolved and subfilter scales from a-priori analysis of direct numerical simulations of isotropic turbulence. *Journal of Turbulence*, *19*(2), 167–197. https://doi.org/10.1080/14685248.2017.1417597

Buzzicotti, M., & Tauzin, G. (2021). Inertial range statistics of the entropic lattice Boltzmann method in three-dimensional turbulence. *Physical Review*, *104*(1), 015302. https://doi.org/10.1103/physreve.104.015302

Callies, J., & Wu, W. (2019). Some expectations for submesoscale sea surface height variance spectra. *Journal of Physical Oceanography*, *49*(9), 2271–2289. https://doi.org/10.1175/jpo-d-18-0272.1

Capet, X., McWilliams, J. C., Molemaker, M. J., & Shchepetkin, A. F. (2008). Mesoscale to submesoscale transition in the California current system. Part III: Energy balance and flux. *Journal of Physical Oceanography*, *38*(10), 2256–2269. https://doi.org/10.1175/2008jpo3810.1

Chassignet, E. P., & Xu, X. (2017). Impact of horizontal resolution (1/12 to 1/50) on Gulf Stream separation, penetration, and variability. *Journal of Physical Oceanography*, *47*(8), 1999–2021. https://doi.org/10.1175/jpo-d-17-0031.1

Chen, R., Gille, S. T., McClean, J. L., Flierl, G. R., & Griesel, A. (2015). A multiwavenumber theory for eddy diffusivities and its application to the southeast Pacific (DIMES) region. *Journal of Physical Oceanography*, *45*(7), 1877–1896. https://doi.org/10.1175/jpo-d-14-0229.1

Contreras, M., Renault, L., & Marchesiello, P. (2023). Understanding energy pathways in the Gulf Stream. *Journal of Physical Oceanography*, *53*(3), 719–736. https://doi.org/10.1175/jpo-d-22-0146.1

Di Leoni, P. C., Alexakis, A., Biferale, L., & Buzzicotti, M. (2020). Phase transitions and flux-loop metastable states in rotating turbulence. *Physical Review Fluids*, *5*(10), 104603. https://doi.org/10.1103/physrevfluids.5.104603

Di Lorenzo, E., Schneider, N., Cobb, K. M., Franks, P. J. S., Chhak, K., Miller, A. J., et al. (2008). North Pacific Gyre Oscillation links ocean climate and ecosystem change. *Geophysical Research Letters*, *35*(8), L08607. https://doi.org/10.1029/2007gl032838

Eyink, G., & Aluie, H. (2009). Localness of energy cascade in hydrodynamic turbulence. I. Smooth coarse graining. *Physics of Fluids*, *21*(11), 115107. https://doi.org/10.1063/1.3266883

Eyink, G. L. (1995). Local energy flux and the refined similarity hypothesis. *Journal of Statistical Physics*, *78*(1–2), 335–351. https://doi.org/10.1007/BF02183352

Eyink, G. L. (2005). Locality of turbulent cascades. *Physica D*, *207*(1–2), 91–116. https://doi.org/10.1016/j.physd.2005.05.018

Ferrari, R., & Wunsch, C. (2009). Ocean circulation kinetic energy: Reservoirs, sources, and sinks. *Annual Review of Fluid Mechanics*, *41*(1), 253–282. https://doi.org/10.1146/annurev.fluid.40.111406.102139

Fox-Kemper, B., Danabasoglu, G., Ferrari, R., Griffies, S., Hallberg, R., Holland, M., et al. (2011). Parameterization of mixed layer eddies. III: Implementation and impact in global ocean climate simulations. *Ocean Modelling*, *39*(1–2), 61–78. https://doi.org/10.1016/j.ocemod.2010.09.002

Fu, L.-L., & Smith, R. D. (1996). Global Ocean circulation from satellite altimetry and high-resolution computer simulation. *Bulletin of the American Meteorological Society*, *77*(1), 2625–2636. https://doi.org/10.1175/1520-0477(1996)077<2625:gocfsa>2.0.co;2

Germano, M. (1992). Turbulence: The filtering approach. *Journal of Fluid Mechanics*, *238*, 325–336. https://doi.org/10.1017/s0022112092001733

Griffies, S. M., Winton, M., Anderson, W. G., Benson, R., Delworth, T. L., Dufour, C. O., et al. (2015). Impacts on ocean heat from transient mesoscale eddies in a hierarchy of climate models. *Journal of Climate*, *28*(3), 952–977. https://doi.org/10.1175/jcli-d-14-00353.1

Grooms, I., Loose, N., Abernathey, R., Steinberg, J., Bachman, S., Marques, G., et al. (2021). Diffusion-based smoothers for spatial filtering of gridded geophysical data. *Journal of Advances in Modeling Earth Systems*, *13*(9), e2021MS002552. submitted. https://doi.org/10.1029/2021ms002552

Haigh, M., Sun, L., McWilliams, J. C., & Berloff, P. (2021). On eddy transport in the ocean. Part I: The diffusion tensor. *Ocean Modelling*, *164*, 101831. https://doi.org/10.1016/j.ocemod.2021.101831

Haigh, M., Sun, L., Shevchenko, I., & Berloff, P. (2020). Tracer-based estimates of eddy-induced diffusivities. *Deep Sea Research Part I: Oceanographic Research Papers*, *160*, 103264. https://doi.org/10.1016/j.dsr.2020.103264

Hendershott, M. (1972). The effects of solid Earth deformation on global ocean tides. *Geophysical Journal International*, *29*(4), 389–402. https://doi.org/10.1111/j.1365-246x.1972.tb06167.x

Hewitt, H. T., Copsey, D., Culverwell, I. D., Harris, C. M., Hill, R. S. R., Keen, A. B., et al. (2011). Design and implementation of the infrastructure of HadGEM3: The next-generation Met Office climate modelling system. *Geoscientific Model Development*, *4*(2), 223–253. https://doi.org/10.5194/gmd-4-223-2011

Jansen, M. F., Adcroft, A., Khani, S., & Kong, H. (2019). Toward an energetically consistent, resolution aware parameterization of ocean mesoscale eddies. *Journal of Advances in Modeling Earth Systems*, *11*(8), 2844–2860. https://doi.org/10.1029/2019ms001750

Kac, M., & Siegert, A. (1947). An explicit representation of a stationary Gaussian process. *The Annals of Mathematical Statistics*, *18*(3), 438–442. https://doi.org/10.1214/aoms/1177730391

Karhunen, K. (1947). Under lineare methoden in der wahr scheinlichkeitsrechnung. *Annales Academiae Scientiarun Fennicae Series A1: Mathematia Physica*, *47*.

Kawabe, M. (1995). Variations of current path, velocity, and volume transport of the Kuroshio in relation with the large meander. *Journal of Physical Oceanography*, *25*(12), 3103–3117. https://doi.org/10.1175/1520-0485(1995)025<3103:vocpva>2.0.co;2

Kelley, D. H., & Ouellette, N. T. (2011). Spatiotemporal persistence of spectral fluxes in two-dimensional weak turbulence. *Physics of Fluids*, *23*(1), 5101. https://doi.org/10.1063/1.3657086

Kessler, W. S. (1990). Observations of long Rossby waves in the northern tropical Pacific. *Journal of Geophysical Research*, *95*(C4), 5183–5217. https://doi.org/10.1029/jc095ic04p05183

Khani, S., & Dawson, C. N. (2023). A gradient based subgrid-scale parameterization for ocean mesoscale eddies. *Journal of Advances in Modeling Earth Systems*, *15*(2), e2022MS003356. https://doi.org/10.1029/2022ms003356

Khani, S., Jansen, M. F., & Adcroft, A. (2019). Diagnosing subgrid mesoscale eddy fluxes with and without topography. *Journal of Advances in Modeling Earth Systems*, *11*(12), 3995–4015. https://doi.org/10.1029/2019ms001721

Khatri, H., Griffies, S. M., Storer, B. A., Buzzicotti, M., Aluie, H., Sonnewald, M., et al. (2023). *A scale-dependent analysis of the barotropic vorticity budget in a global ocean simulation* (Vol. 5). ESS Open Archive. https://doi.org/10.22541/essoar.168394747.71837050/v1

Khatri, H., Sukhatme, J., Kumar, A., & Verma, M. K. (2018). Surface ocean enstrophy, kinetic energy fluxes, and spectra from satellite altimetry. *Journal of Geophysical Research: Oceans*, *123*(5), 3875–3892. https://doi.org/10.1029/2017JC013516

Lea, D., Mirouze, I., Martin, M., King, R., Hines, A., Walters, D., & Thurlow, M. (2015). Assessing a new coupled data assimilation system based on the met office coupled atmosphere–land–ocean–sea ice model. *Monthly Weather Review*, *143*(11), 4678–4694. https://doi.org/10.1175/mwr-d-15-0174.1

Leonard, A. (1974). Energy cascade in large-eddy simulations of turbulent fluid flows. *Advances in Geophysics*, *18*, A237.

Lieb, E. H., & Loss, M. (2001). *Analysis 2nd eq* (Vol. 14). American Mathematical Society.

Linkmann, M., Buzzicotti, M., & Biferale, L. (2018). Multi-scale properties of large eddy simulations: Correlations between resolved-scale velocity-field increments and subgrid-scale quantities. *Journal of Turbulence*, *19*(6), 493–527. https://doi.org/10.1080/14685248.2018.1462497

Loeve, M. (1948). Functions aleatoires du second ordre. In P. Levy (Ed.), *Processus stochastique et mouvement brownien* (pp. 366–420). Gauthier-Villars.

Loose, N., Bachman, S., Grooms, I., & Jansen, M. (2023). Diagnosing scale-dependent energy cycles in a high-resolution isopycnal ocean model. *Journal of Physical Oceanography*, *53*(1), 157–176. https://doi.org/10.1175/jpo-d-22-0083.1

Lorenz, E. N. (1956). *Empirical orthogonal functions and statistical weather prediction* (Vol. 1). Massachusetts Institute of Technology, Department of Meteorology.

Meneveau, C. (1994). Statistics of turbulence subgrid-scale stresses—Necessary conditions and experimental tests. *Physics of Fluids*, *6*(2), 815–833. https://doi.org/10.1063/1.868320

Meneveau, C., & Katz, J. (2000). Scale-invariance and turbulence models for large-eddy simulation. *Annual Review of Fluid Mechanics*, *32*(1), 1–32. https://doi.org/10.1146/annurev.fluid.32.1.1

Muller, C., & Bony, S. (2015). What favors convective aggregation and why? *Geophysical Research Letters*, *42*(13), 5626–5634. https://doi.org/10.1002/2015gl064260
NEMO. (2021). NEMO. [Dataset]. NEMO. https://doi.org/10.48670/moi-00021
O'Rourke, A. K., Arbic, B., & Griffies, S. (2018). Frequency-domain analysis of atmospherically forced versus intrinsic ocean surface kinetic energy variability in GFDL's CM2-O model hierarchy. *Journal of Climate*, *31*(5), 1789–1810. https://doi.org/10.1175/JCLI-D-17-0024.1
Pearson, B., Fox-Kemper, B., Bachman, S., & Bryan, F. (2017). Evaluation of scale-aware subgrid mesoscale eddy models in a global eddy-rich model. *Ocean Modelling*, *115*, 42–58. https://doi.org/10.1016/j.ocemod.2017.05.007
Piomelli, U., Cabot, W. H., Moin, P., & Lee, S. (1991). Subgrid-scale backscatter in turbulent and transitional flows. *Physics of Fluids*, *3*(7), 1766–1771. (ISSN 0899-8213). https://doi.org/10.1063/1.857956
Pope, S. B. (2001). *Turbulent flows*. IOP Publishing.
Pujol, M.-I., Faugère, Y., Taburet, G., Dupuy, S., Pelloquin, C., Ablain, M., & Picot, N. (2016). Duacs dt2014: The new multi-mission altimeter data set reprocessed over 20 years. *Ocean Science*, *12*(5), 1067–1090. https://doi.org/10.5194/os-12-1067-2016
Qiu, B., Chen, S., Klein, P., Wang, J., Torres, H., Fu, L.-L., & Menemenlis, D. (2018). Seasonality in transition scale from balanced to unbalanced motions in the world ocean. *Journal of Physical Oceanography*, *48*(3), 591–605. https://doi.org/10.1175/jpo-d-17-0169.1
Rai, S., Hecht, M., Maltrud, M., & Aluie, H. (2021). Scale of oceanic eddy-killing by wind from global satellite observations. *Science Advances*, *7*(28). (under revision). https://doi.org/10.1126/sciadv.abf4920
Ray, R. (1998). Ocean self-attraction and loading in numerical tidal models. *Marine Geodesy*, *21*(3), 181–192. https://doi.org/10.1080/01490419809388134
Renault, L., Marchesiello, P., Masson, S., & Mcwilliams, J. M. C. (2019). Remarkable control of western boundary currents by eddy killing, a mechanical air-sea coupling process. *Geophysical Research Letters*, *46*(5), 2743–2751. https://doi.org/10.1029/2018gl081211
Richman, J. G., Arbic, B. K., Shriver, J. F., Metzger, E. J., & Wallcraft, A. J. (2012). Inferring dynamics from the wavenumber spectra of an eddying global ocean model with embedded tides. *Journal of Geophysical Research*, *117*(C12), C12012. https://doi.org/10.1029/2012jc008364
Ringler, T., Petersen, M., Higdon, R. L., Jacobsen, D., Jones, P. W., & Maltrud, M. (2013). A multi-resolution approach to global ocean modeling. *Ocean Modelling*, *69*, 211–232. https://doi.org/10.1016/j.ocemod.2013.04.010
Rivera, M. K., Aluie, H., & Ecke, R. E. (2014). The direct enstrophy cascade of two-dimensional soap film flows. *Physics of Fluids*, *26*(5), 055105. https://doi.org/10.1063/1.4873579
Rocha, C. B., Chereskin, T. K., Gille, S. T., & Menemenlis, D. (2016). Mesoscale to submesoscale wavenumber spectra in Drake Passage. *Journal of Physical Oceanography*, *46*(2), 601–620. https://doi.org/10.1175/jpo-d-15-0087.1
Ross, A., Li, Z., Perezhogin, P., Fernandez-Granda, C., & Zanna, L. (2023). Benchmarking of machine learning ocean subgrid parameterizations in an idealized model. *Journal of Advances in Modeling Earth Systems*, *15*(1), e2022MS003258. https://doi.org/10.1029/2022ms003258
Ryzhov, E., Kondrashov, D., Agarwal, N., McWilliams, J., & Berloff, P. (2020). On data-driven induction of the low-frequency variability in a coarse-resolution ocean model. *Ocean Modelling*, *153*, 101664. https://doi.org/10.1016/j.ocemod.2020.101664
Sadek, M., & Aluie, H. (2018). Extracting the spectrum of a flow by spatial filtering. *Physical Review Fluids*, *3*(12), 124610. https://doi.org/10.1103/physrevfluids.3.124610
Satoh, M. (2004). *Atmospheric circulation dynamics and circulation models*. Springer Science & Business Media.
Savage, A. C., Arbic, B. K., Alford, M. H., Ansong, J. K., Farrar, J. T., Menemenlis, D., et al. (2017). Spectral decomposition of internal gravity wave sea surface height in global models. *Journal of Geophysical Research-Oceans*, *122*(1), 7803–7821. https://doi.org/10.1002/2017jc013009
Schlösser, F., & Eden, C. (2007). Diagnosing the energy cascade in a model of the north atlantic. *Geophysical Research Letters*, *34*(2), L02604. https://doi.org/10.1029/2006gl027813
Schubert, R., Gula, J., Greatbatch, R. J., Baschek, B., & Biastoch, A. (2020). The submesoscale kinetic energy cascade: Mesoscale absorption of submesoscale mixed layer eddies and frontal downscale fluxes. *Journal of Physical Oceanography*, *50*(9), 2573–2589. https://doi.org/10.1175/jpo-d-19-0311.1
Scott, R. B., & Arbic, B. K. (2007). Spectral energy fluxes in geostrophic turbulence: Implications for ocean energetics. *Journal of Physical Oceanography*, *37*(3), 673–688. https://doi.org/10.1175/jpo3027.1
Scott, R. B., & Wang, F. (2005). Direct evidence of an oceanic inverse kinetic energy cascade from satellite altimetry. *Journal of Physical Oceanography*, *35*(9), 1650–1666. https://doi.org/10.1175/jpo2771.1
Sogge, C. D. (2008). *Fourier integrals in classical analysis*. Cambridge University Press.
Srinivasan, K., McWilliams, J. C., Molemaker, M. J., & Barkan, R. (2019). Submesoscale vortical wakes in the lee of topography. *Journal of Physical Oceanography*, *49*(7), 1949–1971. https://doi.org/10.1175/jpo-d-18-0042.1
Stanley, Z., Bachman, S., & Grooms, I. (2020). Vertical structure of ocean mesoscale eddies with implications for parameterizations of tracer transport. *Journal of Advances in Modeling Earth Systems*, *12*(10), e2020MS002151. https://doi.org/10.1029/2020ms002151
Stein, E. M., & Weiss, G. (1971). *Introduction to Fourier analysis on Euclidean spaces*. Princeton University Press.
Storer, B. A., & Aluie, H. (2023). FlowSieve: A coarse-graining utility for geophysical flows on the sphere. *Journal of Open Source Software*, *8*(84), 4277. https://doi.org/10.21105/joss.04277
Storer, B. A., Buzzicotti, M., Khatri, H., Griffies, S. M., & Aluie, H. (2022). Global energy spectrum of the general oceanic circulation. *Nature Communications*, *13*(1), 5314. https://doi.org/10.1038/s41467-022-33031-3
Thomson, R. E., & Emery, W. J. (2001). *Data analysis methods in physical oceanography* (3rd ed.). Elsevier Science.
Torres, H. S., Klein, P., Menemenlis, D., Qiu, B., Su, Z., Wang, J., et al. (2018). Partitioning Ocean motions into balanced motions and internal gravity waves: A modeling study in anticipation of future space missions. *Journal of Geophysical Research-Oceans*, *123*(11), 8084–8105. https://doi.org/10.1029/2018jc014438
Trenberth, K. E. (1975). A quasi-biennial standing wave in the southern hemisphere and interrelations with sea surface temperature. *Quarterly Journal of the Royal Meteorological Society*, *101*(427), 55–74. https://doi.org/10.1002/qj.49710142706
Uchida, T., Jamet, Q., Poje, A., & Dewar, W. K. (2021). An ensemble-based eddy and spectral analysis, with application to the Gulf Stream. *Journal of Advances in Modeling Earth Systems*, e2021MS002692. https://doi.org/10.1029/2021MS002692
Uchida, T., Jamet, Q., Poje, A. C., Wienders, N., Dewar, W. K., & Deremble, B. (2023). Wavelet-based wavenumber spectral estimate of eddy kinetic energy: Idealized quasi-geostrophic flow. *Journal of Advances in Modeling Earth Systems*, *15*(3), e2022MS003399. https://doi.org/10.1029/2022ms003399
Vallis, G. K. (2017). *Atmospheric and oceanic fluid dynamics* (2nd ed.). Cambridge University Press.
Vreman, B., Geurts, B., & Kuerten, H. (1994). Realizability conditions for the turbulent stress tensor in large-eddy simulation. *Journal of Fluid Mechanics*, *278*, 351–362. https://doi.org/10.1017/s0022112094003745
Wieczorek, M. A., & Meschede, M. (2018). SHTools: Tools for working with spherical harmonics. *Geochemistry, Geophysics, Geosystems*, *19*(8), 2574–2592. https://doi.org/10.1029/2018GC007529

Wunsch, C. (1991). Global-scale sea surface variability from combined altimetric and tide gauge measurements. *Journal of Geophysical Research*, *96*(C8), 15053–15082. https://doi.org/10.1029/91jc01127

Wunsch, C. (2007). The past and future ocean circulation from a contemporary perspective. *Geophysical Monograph-American Geophysical Union*, *173*, 53.

Wunsch, C., & Stammer, D. (1995). The global frequency-wavenumber spectrum of oceanic variability estimated from TOPEX/POSEIDON altimetric measurements. *Journal of Geophysical Research*, *100*(C12), 24895–24910. https://doi.org/10.1029/95jc01783

Xu, Y., Fu, L.-L., & Tulloch, R. (2011). The global characteristics of the wavenumber spectrum of ocean surface wind. *Journal of Physical Oceanography*, *41*(8), 1576–1582. https://doi.org/10.1175/jpo-d-11-059.1

Youngs, M. K., Thompson, A. F., Lazar, A., & Richards, K. J. (2017). ACC meanders, energy transfer, and mixed barotropic–baroclinic instability. *Journal of Physical Oceanography*, *47*(6), 1291–1305. https://doi.org/10.1175/jpo-d-16-0160.1

Zanna, L., Porta Mana, P., Anstey, J., David, T., & Bolton, T. (2017). Scale-aware deterministic and stochastic parametrizations of eddy-mean flow interaction. *Ocean Modelling*, *111*, 66–80. https://doi.org/10.1016/j.ocemod.2017.01.004

Zhao, D., & Aluie, H. (2018). Inviscid criterion for decomposing scales. *Physical Review Fluids*, *3*(5), 301. https://doi.org/10.1103/physrevfluids.3.054603

Zhao, D., Betti, R., & Aluie, H. (2022). Scale interactions and anisotropy in Rayleigh-Taylor turbulence. *Journal of Fluid Mechanics*, *930*, 1–40. https://doi.org/10.1017/jfm.2021.902